# Nanostructures Based on Cobalt Oxide

Subjects: Nanoscience & Nanotechnology | Engineering, Chemical

Contributor: Gayan W. C. Kumarage

Cobalt oxide (Co3O4) is known to follow the spinel structure as (Co2+)[Co23+O4. The high spin Co2+occupies the interstitial sites of tetrahedral (8a) whereas low spin Co3+are known to occupy the interstitial sites of octahedral (16d) of the close-packed face-centered cubic lattice of CoO.Co2O3. The p-type conductivity of the material (CoO.Co2O3) is known to originate from the vacancies of Co in the crystal lattices or/and excess oxygen at interstitial sites.  Furthermore, 1D nanostructures of Co3O4  have been investigated over the past decades as an active material for chemical analytes detection owing to its superior catalytic effect together with its excellent stability.

cobalt oxide 1D nano structures chemical gas sensor

## 1. Introduction

A chemical sensor is defined as a device that transforms chemical information into an analytically useful signal [1]. Generally, chemical information originate from the chemical reaction of the analyte with the active part of the sensor that induces a variation of the properties of the sensor. However, not only the chemical reaction, but also physical processes (adsorption–desorption), mechanisms of electrical conductivity of a sensitive material, etc., contribute to the overall sensitivity of the sensor [1]. Chemical/gas sensors are identified as excellent candidates for detection and quantification of chemical/gas compounds due to its direct electronic interface, fast response, high sensitivity, and low cost of production [1][2][3][4][5][6][7][8][9]. In general, chemical/gas sensors are based on oxidation or reduction of the active material by the surrounding atmosphere. Numerus types of chemical/gas-sensing materials including metal oxide semiconductors [2][3][4][5][6], conducting polymers [7], conducting polymer composites [8][9], carbon nanomaterials [10], metal oxide/polymer composites [11][12], and various transduction mechanisms have been reported over the past decades.

Metal oxide (MOX) semiconductors may be divided in two different groups depending on their majority carriers. For instance, in n-type MOX semiconductors, such as ZnO, $In_2O_3$, $Fe_3O_2$, $TiO_2$, $WO_3$, $SnO_2$, the majority carriers are electrons, while in p-type, NiO, $Co_3O_4$, $Cr_2O_3$, $Mn_3O_4$, CuO, the majority carriers are holes [13][14][15]. In contrast to n-type MOX gas sensors, p-type MOX ones are less studied, and the reported works are still in a premature stage of development. **Figure 1** shows the results of p-type and n-type MOX gas sensors in Web of Knowledge on 30 June 2021 with the key word “metal oxide gas sensor.” Only 13% articles report on the p-type MOX gas sensors out of a total of 24,234 articles concerning MOX gas sensors. Irrespective of the number of reported works, p-type metal oxides have shown excellent performances in chemical/gas sensing owing to the majority of charge carriers, their conduction paths, resistance to humidity influence on sensing performances, superior catalyst properties, long-term stability, and lower open circuit resistance in contrast to n-type MOX gas sensors [16]. Furthermore, oxygen is excellently adsorbed at p-type MOX surface at low temperature compared to n-type. Thereby p-type MOX gas sensors could potentially be used for the sensing of volatile organic compounds (VOCs) since they are highly oxidized by adsorbed oxygen at the surface compared to surface lattice oxygen [17][18][19]. Moreover, the excellent gas-sensing performances at low working temperatures in p-type MOX gas sensors have paved the interest for the detection and quantification of VOCs [16]. Thereby, the number of scientific research works were gradually increased on p-type MOX as shown in **Figure 2**.

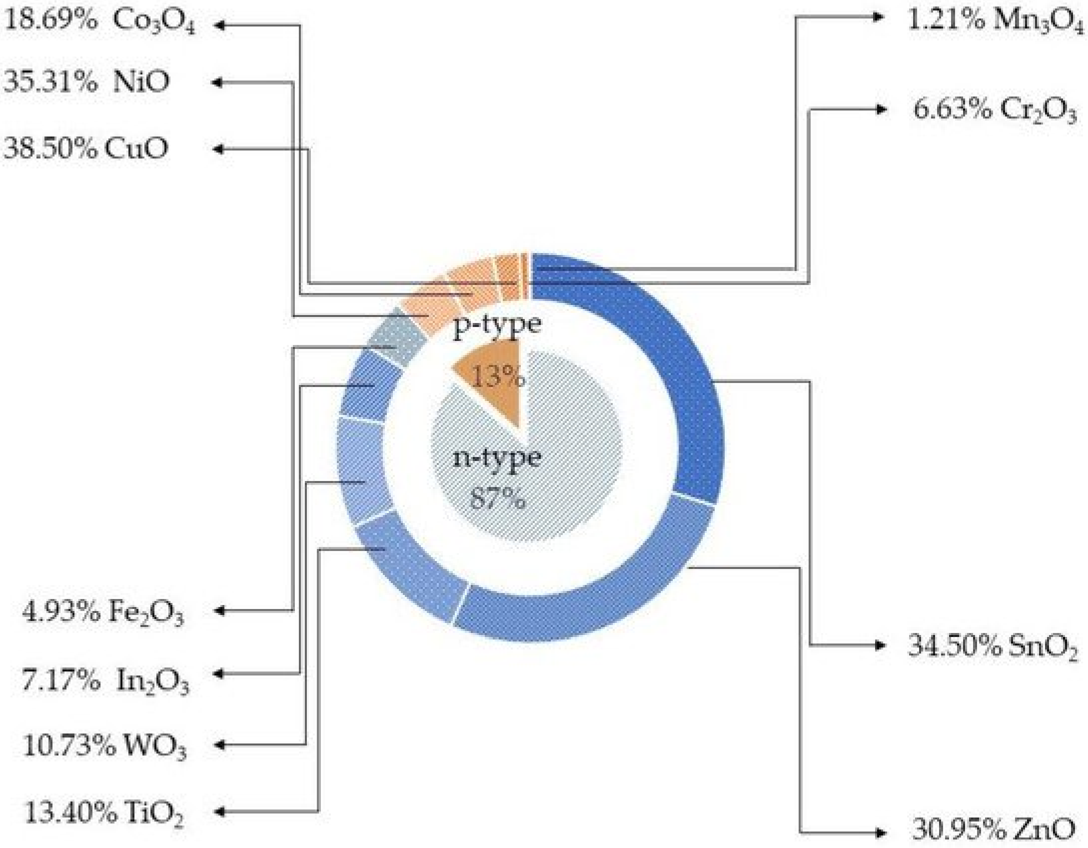

**Figure 1.** The reported scientific research on *n*-type and *p*-type metal oxide gas sensors in Web of Knowledge on 30 June 2021.

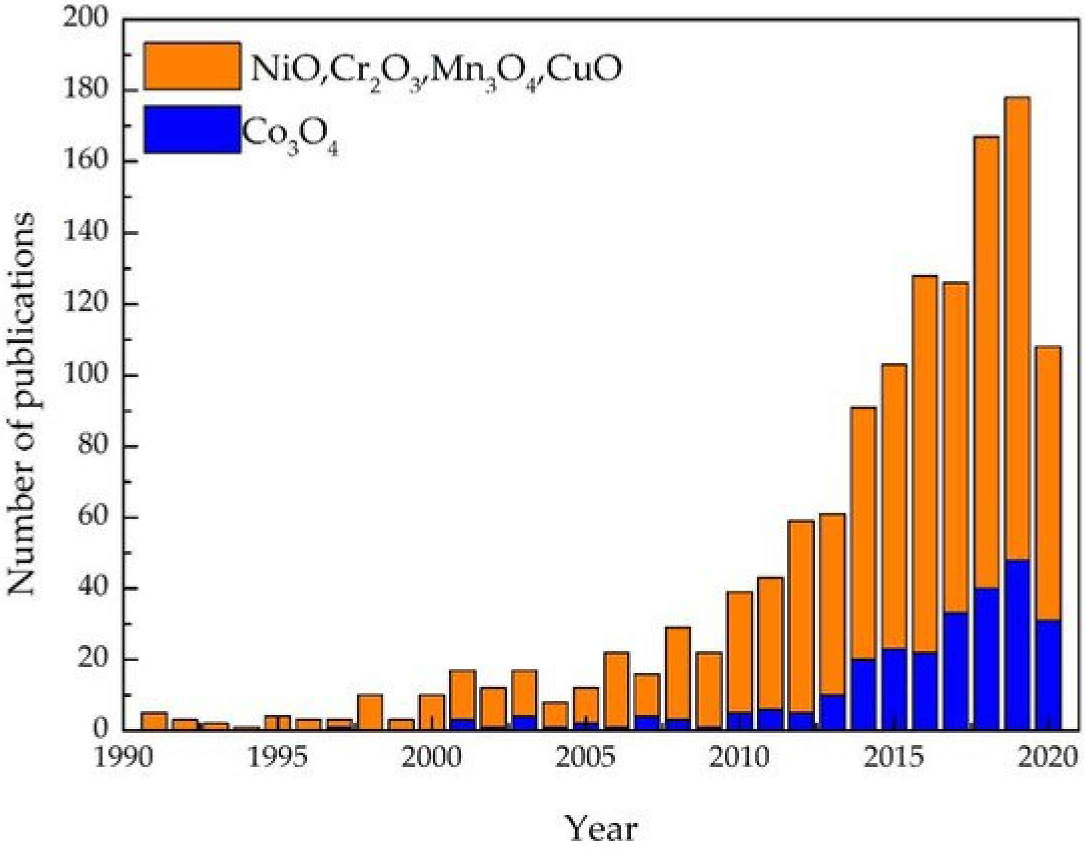

**Figure 2.** The advancement of p-type MOX gas sensors by yearly from the search on Web of Knowledge on 30 June 2021.

Consequently, scientific works on $Co_3O_4$ gas-sensing applications have been gradually increased (**Figure 2**) due to tremendous sensitivity, response/recovery, and stability even at lower and elevated temperatures, superior electrical and chemical properties together with their abundance [20][21]. Similarly, various nanostructures of $Co_3O_4$, nanoparticles [22][23], nanowires [24][25][26][27][28][29], nanorods [30][31], nanosheets [32][33], nanocubes [34], nanoneedles [35], hollow microspheres [36][37][38], urchin-like structures [39][40][41], have been reported in the literature for the detection of $CH_3OH$, $C_2H_5OH$, HCHO, $CH_4$, $CH_3COCH_3$, $C_6H_6$, $C_6H_5CH_3$, $C_6H_5(CH_3)_2$, CO.

However, the significant improvements in the application of one dimensional (1D) nano structures of $Co_3O_4$, on chemical/gas sensing have been attributed to the superior adsorption—desorption of chemical compounds which results in an outstanding response and reliability for chemicals/gases detection [42][43]. Additionally, the higher surface energy, crystalline quality, large intrinsic resistance modulation, number of reactive sites, and large surface to volume ratio of 1D nano structures have significantly improved the gas-sensing performances [14][44]. Though, only two review articles were found on Web of Knowledge database. Review on the 1D nanostructures of $Co_3O_4$ (NWs, NTs, NFs and HNFs) for chemical/gas-sensing applications has not been published yet according to the authors' knowledge. Hence this review is devoted to 1D nanostructures of $Co_3O_4$ and their possible application in chemical/gas sensing. The article initiates with the elementary introduction of $Co_3O_4$ and its gas-sensing ability. Then it flows through the preparation techniques of 1D nano structures of $Co_3O_4$ and its endemic properties significant for chemical/gas sensing. Finally, a comprehensive discussion on the reported 1D $Co_3O_4$ chemical/gas sensors is presented.

# 2. Material and Sensing

Generally, cobalt oxide comprises the spinel structure with an indirect band gap of ~1.5 eV and direct band gap ~2.2 eV. Usual spinel structure is represented by the formula $(A)[B_2]C_4$, in which A and B are cations in tetrahedral and octahedral coordination respectively, whereas C stands for anions. The spinal structure is significantly stable when A is divalent, and B is trivalent for instance $(A^{2+})[B^{3+}]C_4$. Similarly, the cobalt oxide ($Co_3O_4$) is known to follow the spinel structure as $(Co^{2+})[Co_2^{3+}]O_4$ [45]. The high spin $Co^{2+}$ occupies the interstitial sites of tetrahedral (8a) whereas low spin $Co^{3+}$ are known to occupy the interstitial sites of octahedral (16d) of the close-packed face-centered cubic lattice of $CoO.Co_2O_3$ as shown in **Figure 3**a,b. The p-type conductivity of the material ($CoO.Co_2O_3$) is known to originate from the vacancies of Co in the crystal lattices or/and excess oxygen at interstitial sites [45]. However, the charge carriers concentration of the material varies with the operating temperature or doping. $Co_3O_4$ is one of the versatile transition magnetic MOX semiconductors.

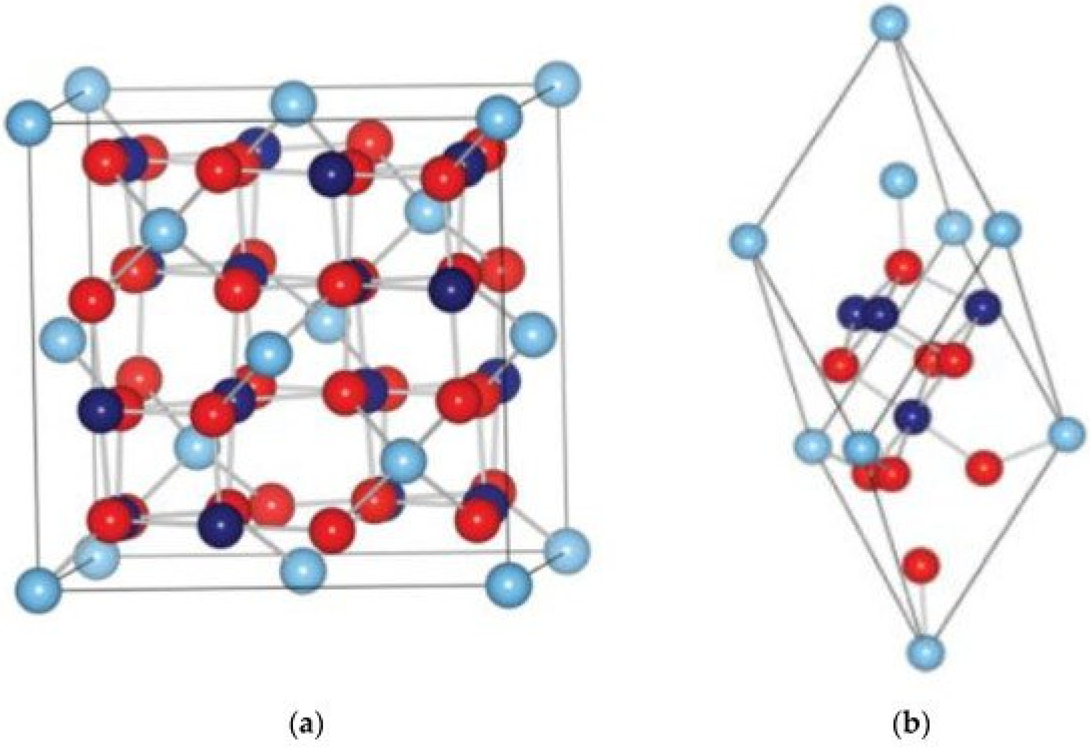

**Figure 3.** Crystal structure of $Co_3O_4$ (**a**) unit cell; (**b**) primitive cell (right). • $Co^{2+}$, • $Co^{3+}$, • $O^{2-}$. Reprinted with the permission from [45].

## 2.1. Characteristics Properties of a Chemical/Gas Sensor

The key parameters that can be useful when discussing chemical/gas sensors are response, selectivity, response time, recovery time, stability, gas detection limit, and operating temperature. A comprehensive but brief understanding on each parameter is useful prior to the detailed discussion on chemical/gas sensors.

*Response* may be described as the fraction of the resistance on the sensing material when interacting with the analyte gas ($R_g$) and the one in air ($R_a$). However, response vastly relies on the crystallite size, porosity, operating temperature, and film thickness. *Selectivity* determines the ability of identifying the target gas in a mixture of gases and can be tuned with the operating temperature. However, MOX chemical/gas sensors may respond in similar manners toward different gas molecules [46]. Hence the selectivity is one of the paramount features when describing the sensing performances. *Stability* is the ability of the active material to keep its properties, such as electrical resistance in case of conductometric sensors, constant over time. *Response time* is an evaluation of the sensors dynamics to achieve a stable value of the monitored sensor parameter, for example the time to accomplish 90% of the final resistance of the sensor when interacting with the gas. Usually, the electrical resistance of a conductometric chemical/gas sensors changes when interacting with the analytes molecules as shown in **Table 1**. In general, a dynamic response curve shows the resistance/conductance variation of the sensor with time. While *the recovery time* may be calculated as the time interval necessary to get back to 90% of the resistance value in air before the gas introduction as the air flow is restored. These parameters can be calculated from the dynamic response plot as shown in **Figure 4**. *Detection limit* is the least concentration of analyte gas that may be detected by the sensor. Lastly, *working temperature* is the temperature where the sensor is operating.

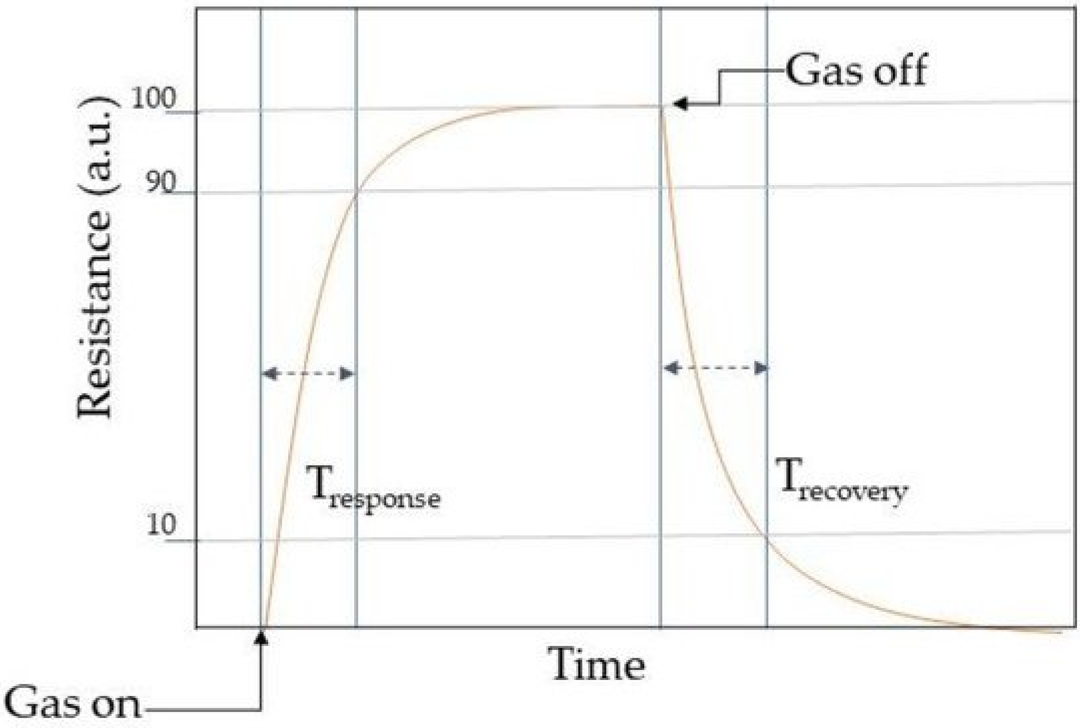

**Figure 4.** Schematic illustration of a dynamic response curve of a conductometric chemical/gas sensor.

**Table 1.** Variation of the resistance in MOX upon the interaction of reducing or oxidizing gases.

| Metal Oxide | Reducing Gases | Oxidizing Gases |
|---|---|---|
| p-type | Resistance increase | Resistance decrease |
| n-type | Resistance decrease | Resistance increase |

## 2.2. Conducting Mechanism of Chemical/Gas Sensor

Chemical/gas sensors comprises two major functions: reception function and transducer function. The reception function is the interaction of the analyte compound with the MOX surface while the transducer mechanism converts the chemical signal into an electronic one in conductometric sensors. Generally, transducing platform is built in planar or tubular design as shown in **Figure 5**a,b. MOX materials are responsible for the receptor function while the entire microstructure comprises the transducer mechanism [47]. However, chemical/gas components absorption at the metal oxide surface relies on imperfections at the surface (valency or coordination of atoms or ions). This absorption is known to be by either weak Van der Waals force (physisorption) or strong chemical bonding by charge exchange process between MOX semiconductor surface and gas analytes (chemisorption). The fundamental working principle of conductimetric chemical/gas sensor is based on this interaction and its effect on the sensor resistance. It is interesting to describe the working principle behind the electrical resistance modification of MOX in spite of the summary reported by the Moseley et al. (**Table 1**) [48].

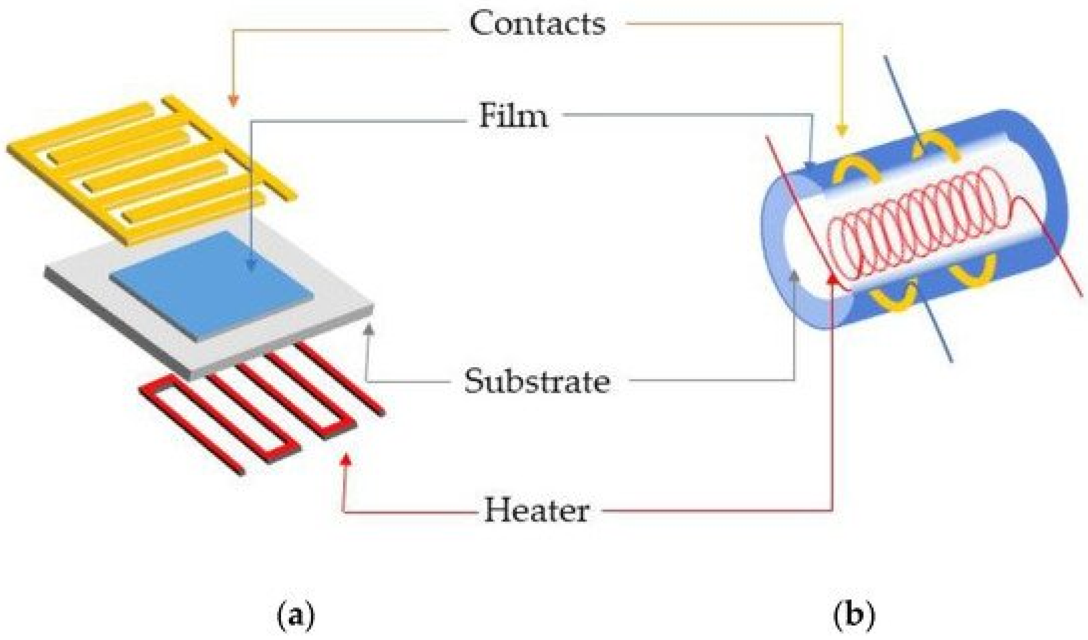

**Figure 5.** Two types of transducing platforms: (**a**) planar; (**b**) tubular configuration.

The electrical conduction in a chemical gas sensor is based on charge carriers (electrons for n-type and hole for p-type MOX gas sensors). However, the ionosorbed species on MOX surface play also a key role in the electrical conduction since these sensors are working in ambient environment. In this scenario, oxygen and water vapors are the prominent. Concerning oxygen adsorption, molecular $O_2^-$, atomic $O^-$, and $O^{2-}$ species are present at the temperatures < 150 °C, 150–400 °C, and >400 °C respectively and the chemical routing is shown in Equations (1)–

(3) [11][14]. When oxygen ions are chemisorbed, free charge carriers (holes) concentration increase in p-type materials such as $Co_3O_4$. These chemisorbed oxygen species are responsible for electron trapping from MOX valance band, forming an electronic core shell as depicted in **Figure 6** [14]. This may result in a hole-accumulating layer (HAL) near the semiconductor surface [14]. The formed HAL is crucial for the receptor/transduction function. Additionally, in p-type MOX semiconductors electrical conduction is through the semiconducting near surface regions (parallel path conduction) [14][49]. A detailed description on conductive model on p-type metal oxide is found in Barsan et al. and Kim et al. [14][49].

$$O_{2(ads)} + e^- \rightarrow O_2{}^-{}_{(ads)} \quad (1)$$

$$O_2{}^-{}_{(ads)} + e^- \rightarrow 2O^-{}_{(ads)} \quad (2)$$

$$2O^-{}_{(ads)} \rightarrow O^{2-}{}_{(ads)} \quad (3)$$

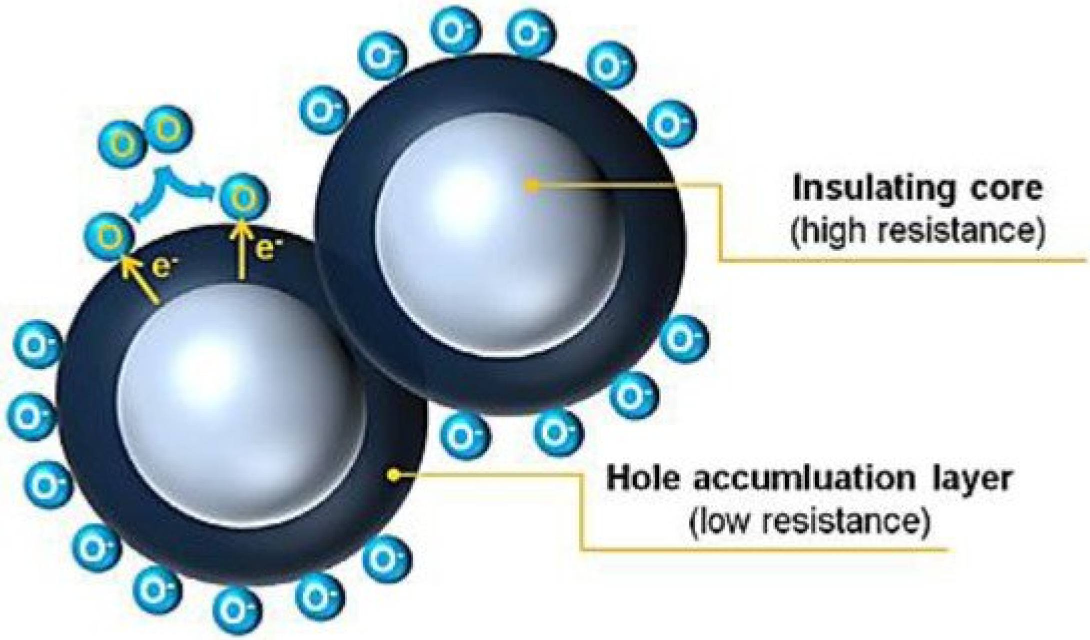

**Figure 6.** The electronic core–shell structures in p-type oxide semiconductors suggested by Kim et al. Reprinted with the permission from [14].

In addition to the conduction model by Barsan et al. an overlook on the MOX band structure modification with the chemisorption of these species could be interesting. **Figure 7**a depicts the band structure prior to any surface reaction. Once oxygen is ionosorbed on the MOX surface, electron from the valence band are captured on the surface traps. This process alters the hole concertation in the accumulation layer resulting in upward band bending as represented in **Figure 7**b. Subsequently, the electrical resistance of the hall accumulation layer decreases [49]. The interaction of the reducing gas with sensing material may increase the HAL resistance due to the consumption of ionosorbed species. This results in the decrease of the hole concentration causing a downward band bending as in **Figure 7**c. Furthermore, direct adsorption of oxidizing species, such as highly electronegative $NO_2$, can also alter the MOX electrical conductance and a detailed explanation has been reported in Comini et al. [5]. Additionally, energy band bending due to the electron transfer between the semiconducting material and the chemical compounds, formation of Schottky barriers, microstructure of the MOX semiconductor also influence the electrical resistance [47][50].

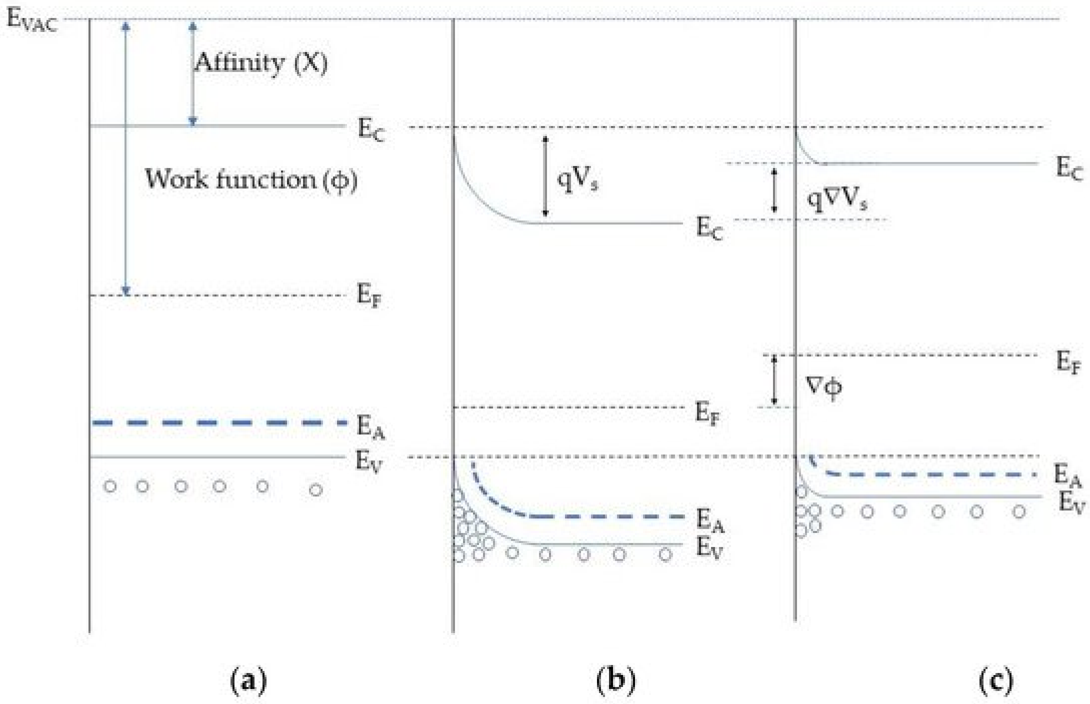

**Figure 7.** Energy bands structure at the near surface when interacting with oxygen and reducing gases: (**a**) prior to any surface interaction; (**b**) electrons trapping and formation of the holes accumulation layer due to oxygen adsorption; (**c**) the decrease of the surface charge due to the interaction with the reducing gas; $E_C$–conduction band position, $E_F$–Fermi level position, $E_C$–valance band position, q- electron charge, $qV_S$- potential barrier.

The net electrical resistance of the gas-sensing element is the total resistance of the combination of three regions; (a) metal-semiconductor, (b) semiconductor-semiconductor, and (c) semiconductor metal junctions. There are therefore four types of resistance:

- Metal to semiconductor;
- Outer conductive and narrow accumulation layers at the surface of the nanowire;
- Narrow accumulation layers at the surface of the grains and broad bulk of the nanowire;
- Nanowire to nanowire.

By assuming constant resistance and capacitance values in these four types of resistance described above irrespective of gases interaction, a detailed explanation on the conductance is provided based on DC equivalent circuit by Barsan et al. in the specific case of granular materials [49].

Considering all these facts, synthesis of 1D nano structures for the chemical/gas sensing has attracted the researchers' attention for sensitivity and response improvements by reducing the resistance in the large number of contacts regimes mentioned above.

In general, the electron momentum in 1D nanostructures is confined in two directions which in turn force electron motion in one direction. However, the electrical transport phenomena in 1D nano structures may be described using the cylindrical approach of Poisson equation [49][50]. The limitation on the electrical conduction length is varying depending on the formation of the space charge layer (depletion layer or hole accumulation layer in n-type or p-type metal oxide semiconductor respectively) due to the ionosorption species as shown in **Figure 8**a,b. Nevertheless, the transport mechanism should be revised when the grain size (dm) becomes low compared to the Debye length ($\lambda_D$). In the instance of a large grain, (grain size, $d_m$ >> thickness of the space charge layer, $2\lambda_D$), the conductance is limited by Schottky barrier at grain boundaries. Once, $d_m = 2\lambda_D$, conductance is limited by necks between the grain, while the conductance is highly affected by each grain once $d_m < 2\lambda_D$ [46]. This may account for specific effects along the nano structure which is known to be the main reason for significant alterations in its electrical properties.

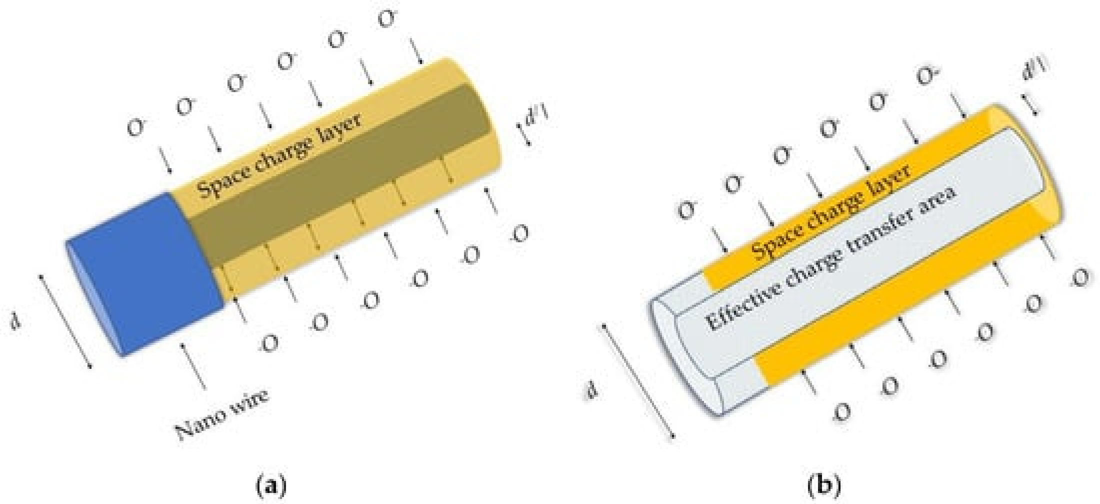

**Figure 8.** Graphical representation: (**a**) nano wire diameter higher than Debye length and space charged layer; (**b**) cross section of the nano wire and space charged layer. d is the diameter of the nano wire and the $d^{/}$ is the width of the space charge layer.

## 3. Growth Techniques of 1D Nano Structures of the $Co_3O_4$

In general, bottom-up or top-down approaches are used for the nano structures growth [51]. The experimental setup for bottom-up approaches may be low cost producing high crystallinity and purity nanostructures, but their alignment may be extremely difficult. Top-down approaches suffer from long preparation times, while they easily form structures directly on flat substrates. Concerning the growth of $Co_3O_4$ nano structure as chemical/gas sensors, several growth techniques such as hydrothermal [15][16][22][23][24][34][52][53], electrospinning [54], and solvothermal [3][27][55][56] were widely employed. Thereby a brief description of each growth techniques will be made.

## 3.1. Hydrothermal and Solvothermal Techniques

The hydrothermal and solvothermal techniques are the topmost attracting methods for fabricating nanostructured materials owing to high yield, uniform products, low energy consumption, lower pollution, easy control together with simple manipulation [57]. In general, both the methods are similar. Hydrothermal process is carried out in aqueous medium above the boiling point. Solvothermal occurs in a nonaqueous (mainly organic phase) solution at quite high temperatures. Both the techniques are executed in steel autoclaves with or without Teflon liners under specific growth conditions such as pressure, temperature, reactant concentration, and duration which are known to tune morphology and crystal structure as shown in **Figure 9**a–h. Additionally, a comprehensive comparison on each method is found in Wang et al. [58].

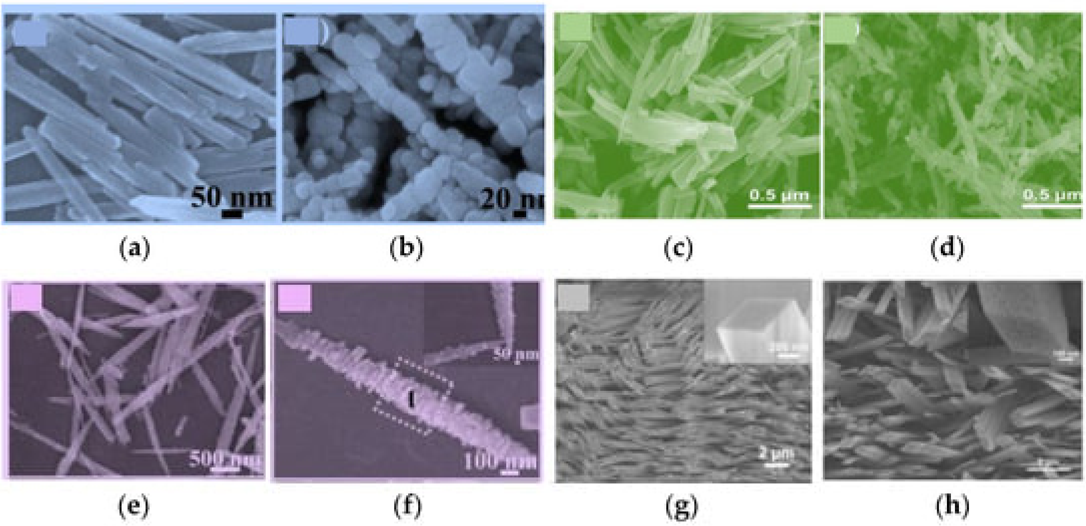

**Figure 9.** The SEM microgram hydrothermally grown $Co_3O_4$ nano structures: (**a**,**b**), nanoparticles-assembled $Co_3O_4$ nanorods, reprinted with the permission from [27]; (**c**,**d**) Cr-doped $Co_3O_4$ nanorods, reprinted with the permission from [59]; (**e**,**f**) hierarchical nanorods, reprinted with the permission from [53]; (**g**,**h**) rhombus-shaped nanorod arrays, reprinted with the permission from [25].

## 3.2. Electrospinning Techniques

Electrospinning technique is performed injecting a liquid precursor solution via a spinneret. In general, high electrical voltage difference is applied between the liquid precursor and the collector, which leads to an extrude on the solution forming a jet from the nozzle. The jet-formed fibers are deposited on the collector [46]. This method of growing nano structures with higher length is simple and flexible specially for the nano fibers' growth. However, electrospinning is controlled by several parameters, such as operating voltage, viscosity, pressure, flow rate, and temperature [60]. Presently, two standard electrospinning setups are available; horizontal and vertical and a comprehensive study on electrospinning techniques is found in Bhardwaj et al. [61]. Additionally, a post growing heat treatment is essential in the electrospinning technique to eliminate the solvent and to solidify the nano structures. **Figure 10**a,b shows the general electrospinning setup and **Figure 10**c–f the SEM images of different achieved $Co_3O_4$ NFs. However, with the advancement of this technology, some research groups have introduced state-of-the-art systems that can grow more graded nano fiber structures at higher efficient and controllable means.

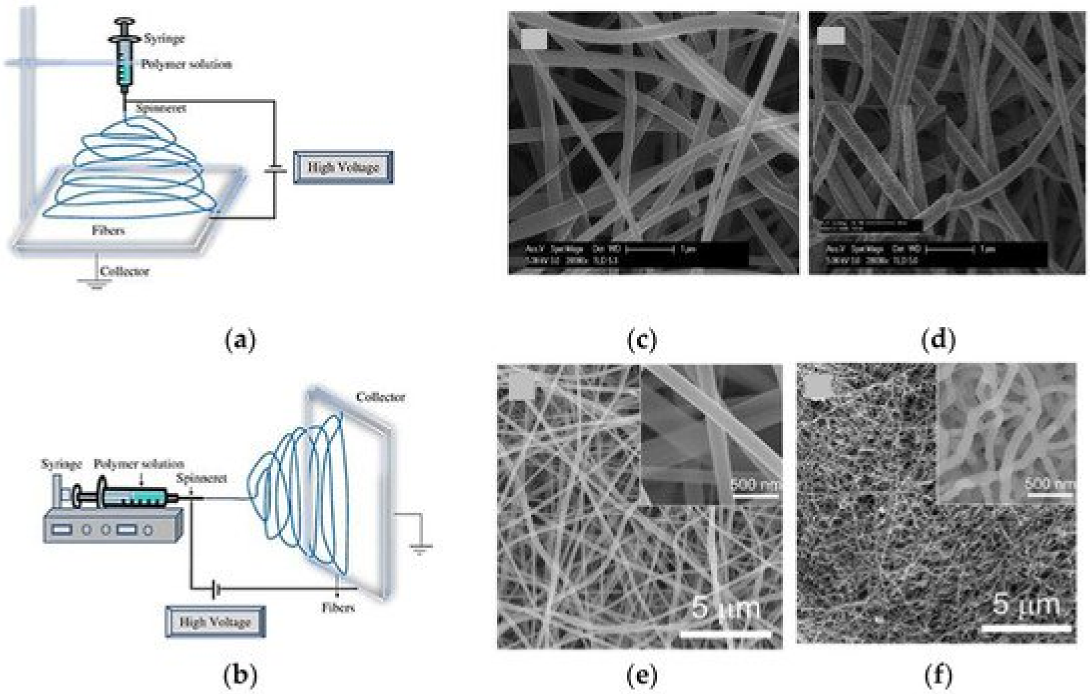

**Figure 10.** Experimental setup of electrospinning technique: (**a**) vertical; (**b**) horizontal, reprinted with the permission from [61]; (**c**,**d**) nano structure obtained via eletrospun technique, reprinted with the permission from [62]; (**e**,**f**) nano structure obtained via eletrospun technique, reprinted with the permission from [63].

## 4. Overview of Reported 1 D Nano Structured $Co_3O_4$ Gas Sensors

In general, variation of the electrical resistance over the course of the analyte interaction (reducing or oxidizing) on the MOX surface can be used to study the gas-sensing performances of the MOX hence to detect the target gas [64]. However, $Co_3O_4$ 1D nano structures sensors are still capable of detecting few gases such as CO, $H_2S$, $NH_3$, and some VOCs. Among these, $C_2H_5OH$ and $C_3H_6O$ are the frequently reported. **Table 2** shows the reported studies of $Co_3O_4$ 1D nano structures as chemical/gas sensors.

**Table 2.** Summary of gas-sensing performance of the reported 1D nano structures of $Co_3O_4$ gas sensors.

| $Co_3O_4$ Morphology | Synthesis Procedure | Analyte Gas | Concentration (ppm) | $T_{op}$ (°C) | Response | $T_{res}$ (s) | $T_{rec}$ (s) | Reference |
|---|---|---|---|---|---|---|---|---|
| Nanorods | Solvothermal | $C_2H_5OH$ | 100 | 300 | 25.7 $^a$ | 29 | 10–13 | [3] |

| $Co_3O_4$ Morphology | Synthesis Procedure | Analyte Gas | Concentration (ppm) | $T_{op}$ (°C) | Response | $T_{res}$ (s) | $T_{rec}$ (s) | Reference |
|---|---|---|---|---|---|---|---|---|
| Nanorods | Coprecipitation | CO | 50 | 250 | 6.5 [b] | NA | NA | [15] |
| Nano wires | Hydrothermal | CO | 20 | 100 | 13.5 [b] | 62.5 | 100 | [16] |
| Nanowires | Hydrothermal | $C_6H_{15}N$ | 100 | 250 | 4 [b] | NA | NA | [22] |
| Nanowires | Hydrothermal | $C_3H_6O$ | 150 | 200 | 23 [b] | NA | NA | [23] |
| Nanorods | Hydrothermal | $C_3H_6O$ | 74570 | 300 | 18.5 [c] | 40 | 180 | [24] |
| Rhombus shaped nanorod | Hydrothermal | $C_2H_5OH$ | 500 | 160 | 71 [b] | 90 | 60 | [25] |
| Nanorods | Solvothermal | $C_7H_8$ | 200 | 200 | 35 [b] | 90 | 55 | [27] |
| Nanorods | Hydrothermal | $(C_2H_5)_2O$ | 100 | 160 | 110.34 [c] | NA | NA | [30] |
| Nano needles | Hydrothermal | $C_2H_5OH$ | 130 | 100 | 89.6 [b] | NA | NA | [34] |
| Hierarchical Nanofiber | Hydrothermal | $C_3H_6O$ | 100 | 190 | 9.3 [b] | 7 | 1 | [52] |
| Hierarchical nanorods | Hydrothermal | $NH_3$ | 100 | 160 | 11.2 [b] | 2 | 10 | [53] |
| Cr-doped nanorods | Solvothermal | $C_7H_8$ | 5 | 250 | 17 [b] | NA | NA | [59] |
| | | $C_8H_{10}$ | | | 18 [b] | NA | NA | |
| Nanofiber | Electrospinning | CO | 5 | 100 | 2.4 [b] | 14 | 36 | [62] |
| Nano Fiber | Electrospinning | $C_2H_5OH$ | 100 | 300 | 22.1 [b] | NA | NA | [63] |
| Nano Fiber | Electrospinning | $C_2H_5OH$ | 100 | 301 | 51.2 [b] | 16 | 8 | [65] |
| Composite nanofiber | Electrospinning | $C_3H_6O$ | 5 | 300 | 2.29 [b] | NA | NA | [66] |
| Nano Fiber | Electrospinning | $C_8H_{10}$ | 100 | 255 | 10.6 [a] | 15 | 22 | [67] |
| Nano chains | Hydrothermal | $H_2S$ | 100 | 300 | 4.3 [b] | 46 | 24 | [68] |
| Nano tubes | Facile solution route | HCHO | 50 | 180 | 6.3 [b] | 3 | 1 | [69] |
| $Co_3O_4$/CuO nanotubes | Electrospinning | $C_3H_2F_6O$ | 0.5 | 90 | 8.8 [b] | 7.3 | 5.2 | [70] |

| $Co_3O_4$ Morphology | Synthesis Procedure | Analyte Gas | Concentration (ppm) | $T_{op}$ (°C) | Response | $T_{res}$ (s) | $T_{rec}$ (s) | Reference |
|---|---|---|---|---|---|---|---|---|
| Composite nanofiber | Electrospinning | $NH_3$ | 50 | RT | 53.6 $^c$ | 4 | 300 | [71] |

Note: Top = operating temperature; Tres = response time; Trec = recovery time; NA = not available; a = Ra/Rg; b= Rg/Ra; c = (Rg−Ra/Ra).

## 4.1. Sensing toward Ethanol (C2H5OH)

Ethanol is a VOC that is vastly present in the daily life of human beings in means of food, beverages, fuel-processing, pharmaceutical, as well as in many laboratories and industries for diverse research and applications [72]. However, the long-term exposure to $C_2H_5OH$ has been identified as the main reason for serious health effects such as lethargy, irritation to skin and eye, difficulty breathing, coma, liver damage, and intoxication. Moreover, $C_2H_5OH$ as alcoholic drink has been identified as one of the root causes for the rising traffic accidents around the world [73]. For this reason, almost all countries have legalized the consumption limitation of $C_2H_5OH$. For example, in Italy the highest ethanol level that is allowed in the breath of drivers is 130 ppm (0.05% in blood) while in the USA, 208 ppm (0.08% in blood) [74]. Hence, detection and quantification of $C_2H_5OH$ in environment as well as in human breath have become a necessity. Before discussing the $C_2H_5OH$-sensing applications it would be interesting to understand its sensing mechanism at MOXs surface. When ethanol is interacting with the near surface irrespective of the type of MOXs sensor, these molecules are chemisorbed on the MOXs surfaces. Afterwards, chemisorbed ethanol molecules start to react with the adsorbed oxygen species resulting in the formation of $H_2O$ and $CO_2$. Hence the trapped electrons are liberated back to the MOXs altering the sensor resistance. The chemical reaction between $C_2H_5OH$ and adsorbed oxygen species on the near surface of the MOXs is described as in (4–5) regardless of the type of the MOXs [74].

$$C_2H_5OH_{(ads)} + O^{-}_{(ads)} \rightarrow CH_3CHO_{(ads)} + H_2O + e^{-} \quad (4)$$

$$CH_3CHO_{(ads)} + 5O^{-}_{(ads)} \rightarrow 2CO_2 + 2H_2O + 5e^{-} \quad (5)$$

Among the synthesis techniques for $Co_3O_4$ NRs preparation, solvothermal technique one has been used to prepare $C_2H_5OH$-sensing devices by Choi et al. in 2010 [3]. The integrated sensors by the Choi et al. have demonstrated a superior selectivity and response to 100 ppm of $C_2H_5OH$ compared to that of $H_2$ and CO at 300 °C. Furthermore, the effective and prompt diffusion of gases onto the whole surface $Co_3O_4$ nanorods give rise to a superior response of 25.4 ($R_a/R_g$) to 100 ppm $C_2H_5OH$ together with the response time of 29 s and recovery time of 10–13 s compared to the one of nano cubes and particles [3].

It is known that the morphology of the nano structures can be altered depending on the original material, the growth technique, and its parameters. Wen et al. in 2013 have addressed the growth of $Co_3O_4$ rhombus-shaped NRs on polycrystalline alumina ceramics plate, investigating their $C_2H_5OH$ detection capabilities [25]. They have also demonstrated the necessity of post treatment annealing step for the hydrothermal-assisted growth. This additional step is known to support the removal of adsorbed water molecules upon calcination [25]. Wen et al. have shown the absence of FTIR peaks of O-H (3574 $cm^{-1}$ and 1635 $cm^{-1}$), O-H groups interacting with fluoride (3417 $cm^{-1}$), Co-OH (995 $cm^{-1}$), and Co-F (734 $cm^{-1}$) vibrations in the calcinated sample compared to that of the as-grown one (**Figure 11**a). Additionally, dehydration and lattice contraction may also occur during the thermal treatment, causing a topology modification of more rough surfaces (**Figure 11**b,c). Furthermore, the rougher topology along with the unique structure of $Co_3O_4$ NR arrays, the high surface to volume ratio, the actual participation of each NR for the gas sensing due to the direct growth of $Co_3O_4$ NRs on substrates and the space between individual NRs has been identified as the main roots of outstanding sensing performances [25]. Moreover, these unique features have also tuned the sensor toward breath analysis application and extended stability [25].

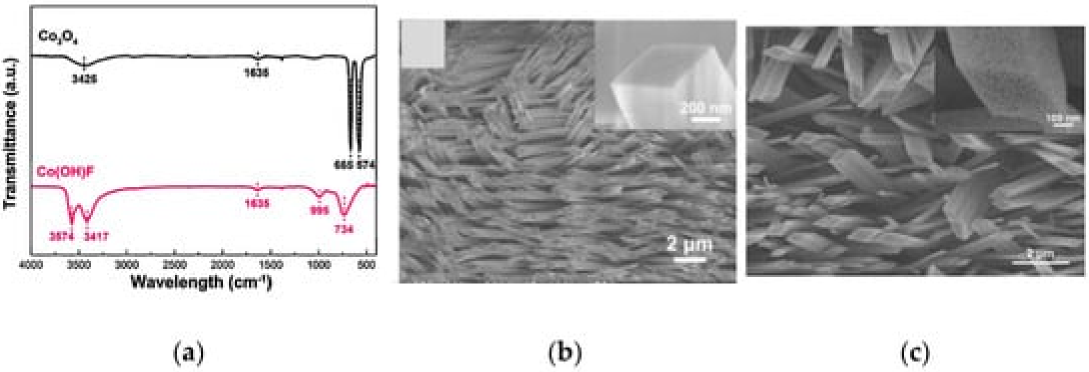

**Figure 11.** FTIR spectra of the $Co_3O_4$ NRs: (**a**) before and after sintering at 450 °C; (**b**) SEM images of Co(OH)F NR; (**c**) SEM image of the rhombus-shaped $Co_3O_4$ NR arrays annealed at 450 °C. Reprinted with the permission from [25].

Nguyen et al. have reported the occurring of rough and porous nature in the topology on the NRs upon the calcination [24]. However, the porous morphology has been attributed to the oxidation of $Co(OH)_x(CO_3)_{0.5}.0.11H_2O$ in the as grown material. Furthermore, Nguyen et al. have observed the necessity of higher amount of oxygen vacancies [Equations (4)–(6)] for an effective ethanol detection. $Co_3O_4$ NRs sensors show higher responses toward ethanol at 300 °C in ambient air compared to $N_2$ environment due the reduction of pre-adsorbed oxygen in the $Co_3O_4$ in $N_2$ environment.

Electrospinning has been employed for the preparation of nano fibers (NFs) for the detection of $C_2H_5OH$ by Yoon et al. [65]. The sensors have shown superior sensitivity ($R_g/R_a = 51.2$) toward 100 ppm of $C_2H_5OH$ compared to CO, $C_3H_8$, and $H_2$ at 301 °C before decreasing to 19.2 at 336 °C. While the recovery time was decreasing as the operating temperature increases due to the thermal boosting of oxygen ionization.

Furthermore, Yoon et al. have demonstrated the effect of NFs dimension in the sensing properties in 2014 [63]. In the reported study three sets of NFs were grown by altering the ultrasound sonication time using the electrospinning followed by calcination. The sensor resistance has been found to increase with the sonication time due to the reduction of the effective surface area. This decrement resulted from the breaking of well-connected long nanofibers into less connective nanoparticles or shorter fibers. Additionally, the variation in the contact area among the particles has been identified as a possible reason for the decrease in the response with higher duration of sonication. Hence, the inter-particle connectivity could be a significant parameter for the gas-sensing performances in $Co_3O_4$ devices.

The detection of lower concentrations is highly beneficial when considering safety applications. One successful study has reported the detection of 10 ppm $C_2H_5OH$ exploiting needle shaped $Co_3O_4$ nano arrays (**Figure 12**a) that were grown in facile hydrothermal route by Wen et al. in 2014 [34]. The reported nanoneedles array has demonstrated mesoporosity and quasi-single-crystalline structure which has been identified as the main motivation for the superior response of 89 ($R_g/R_a$) toward 100 ppm ethanol at a working temperature of 130 °C (**Figure 12**b). Furthermore, several other key factors, such as the strong adhesion between the sensing materials and the substrates, which in turn improve the good ohmic contact, the random orientation of the nanoneedle arrays and the special exposed crystal planes of $Co_3O_4$ have been ascribed for the superior sensing performance and their stability.

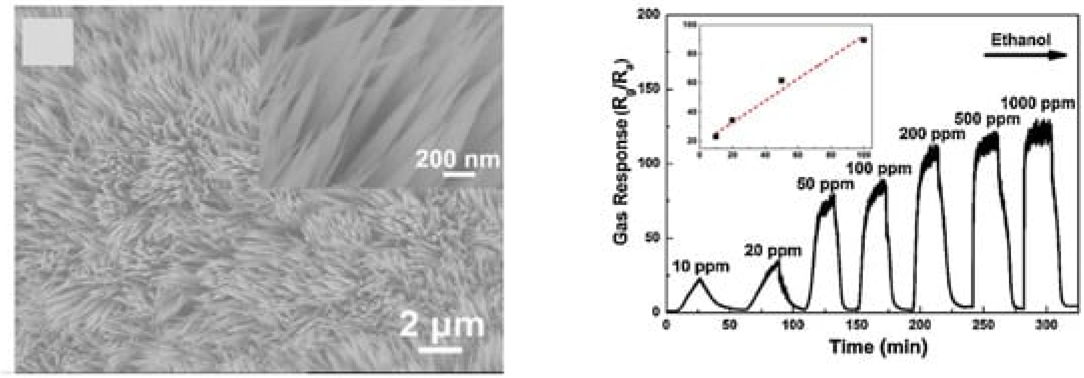

(a) (b)

**Figure 12.** The SEM image of $Co_3O_4$: (**a**) nanoneedle arrays; (**b**) the dynamic response and recovery plot of the $Co_3O_4$ toward ethanol. Reprinted with the permission from [34].

## 4.2. Sensing toward Acetone ($C_3H_6O$)

Acetone is a VOCs known to be caused by irritation to nose, eyes, throat, and central nervous system as the concentration is higher than 173 ppm or if the exposure continues for several hours [60][72]. Moreover, it has been identified as a key compound to identify health issues in human body by analyzing the human breath [67][75]. Hence, the detection of acetone is essential for both society safety and health. An illustration of $C_3H_6O$ detection mechanism on nanofibers is shown in **Figure 13** [52]. A superior sensitive and selective performance toward acetone has been reported by Choi et al. on $Co_3O_4$ NFs composite with Ir NPs and graphene oxide (GO) sheets in 2014 [66]. $Co_3O_4$ NFs, have been grown by electrospinning technique while the GO sheets as well as Ir NPs were grown by the polyol method [68]. The composites NFs (1 wt% Ir-GO-$Co_3O_4$) were able to detect acetone even at 120 ppb in highly humid ambient conditions (90% RH) demonstrating great potentialities for acetone analysis in human breath [66]. In addition, the sensors have shown excellent selectivity toward acetone other than the usual breath biomarkers; pentane, $NO_2$, NO, $NH_3$, and CO. One of the reasons for these excellent performances is the combined catalytic effect of GO sheets and Ir NPs. A second one is the hole accumulation layer thinning on the surface of $Co_3O_4$ NFs due to Ir NPs together with the effective electronic sensitization by the GO sheets. In addition, the rapid transfer of carrier to the sensing electrodes, due to the highly conductive GO sheets, contributed to improve the performances.

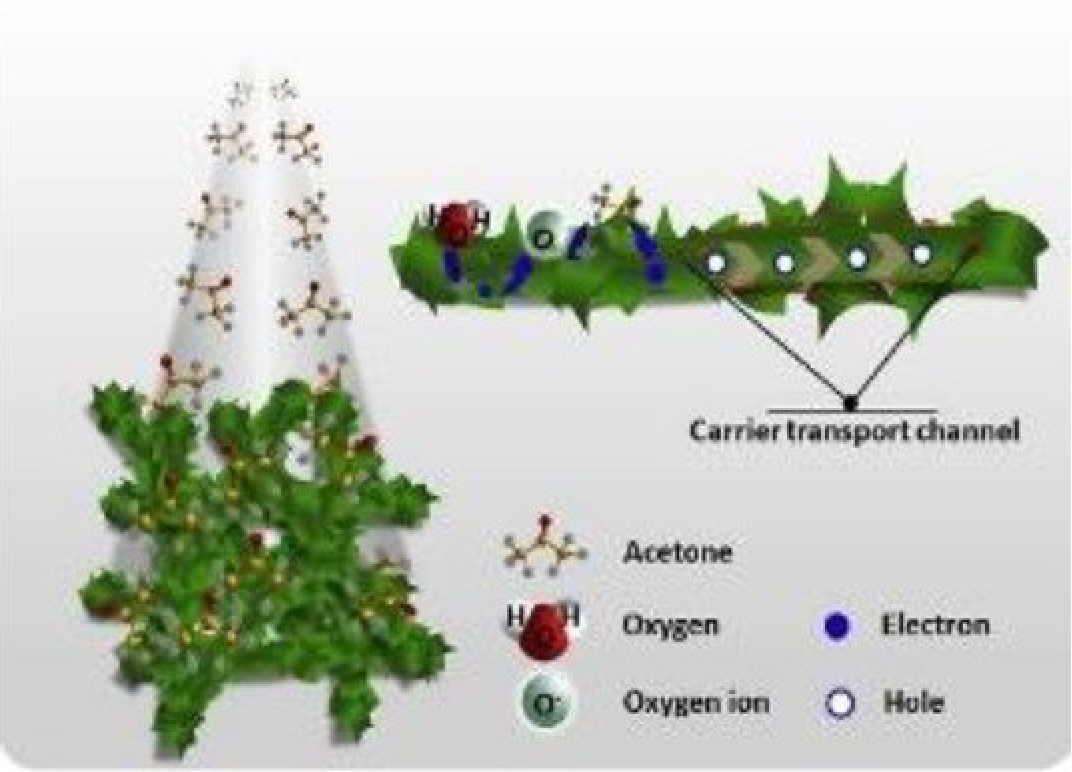

**Figure 13.** The illustration of sensing mechanism of $C_3H_6O$ on $Co_3O_4$. Reprinted with the permission from [52].

Another interesting morphology for chemical compounds detection is one of the hierarchical nanofibers (HNF). Its effective surface area is outstanding and there is a smooth transfer of carriers through nanofibers without additional barriers, due to the connection of the nanosheet-like structures in the nanofiber [52]. In 2019 Cao et al. have demonstrated $C_3H_6O$ sensing with HNFs at an operating temperature of 190 °C. The grown HNFs comprised many nanosheets with smooth surface almost perpendicular to the nanofiber's surfaces (thickness of 20–40 nm) as shown in **Figure 14**a–c [52]. However, Zhang et al. have reported the possibility of detecting $C_3H_6O$ at an operating temperature of 75 °C with $Co_3O_4$ NWs assembled on hollow carbon spheres ($Co_3O_4$ NW-HCS) [23]. The enhanced sensing performances at low operating temperature have been attributed to the interaction between hollow carbon spheres and short $Co_3O_4$ nanowires. Moreover, the unique porous cavity structure of hollow carbon spheres is contribute to the excellent sensing performances by paving higher number of available sites for easy adsorption and desorption of $C_3H_6O$ molecules.

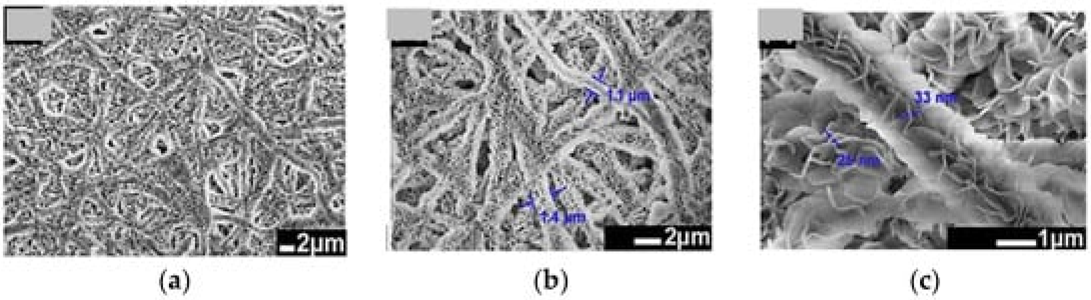

**Figure 14.** The SEM micrograms: (**a**–**c**) HNF of $Co_3O_4$. Reprinted with the permission from [52].

## 4.3. Sensing toward Carbon Monoxide (CO)

The World Health Organization has announced that 92% of the world's population live in zones with poor air quality [69]. Consequently, the lack of air quality has been identified as the reason for the increment of the premature death worldwide [69]. CO is one of the major air pollutants. It is a byproduct of the incomplete combustion process of fossil fuels, from power stations (coal), industrial factories, and vehicle exhaust. CO is colorless, tasteless, poisonous, and odorless [70]. CO has a greater affinity with hemoglobin compared to $O_2$. Thereby, CO binds easier than $O_2$ to hemoglobin as it enters into the blood which in turn results in suffocation to death [71]. Hence CO monitoring in living environments is significantly valuable. $Co_3O_4$ 1D nano structures growth for the detection of CO may be interesting due to its long-term stability, high surface/volume ratio, and low-temperature operation [16]. **Figure 15** shows the interaction of CO on the MOX surface. The sensing reactions can be written as in Equations (6)–(9) [64].

$$CO_{(g)} \rightarrow CO_{(ads)} \text{ (6)}$$

$$CO_{(ads)} + O^- \rightarrow CO_2 + e^- \text{ (7)}$$

$$CO + OH^-_{(ads)} \leftrightarrow HCO_2^- \leftrightarrow H^+_{(ads)} + CO_2 + 2\,e^- \text{ (8)}$$

$$CO + H_2O \rightarrow CO_2 + H_2 \text{ (9)}$$

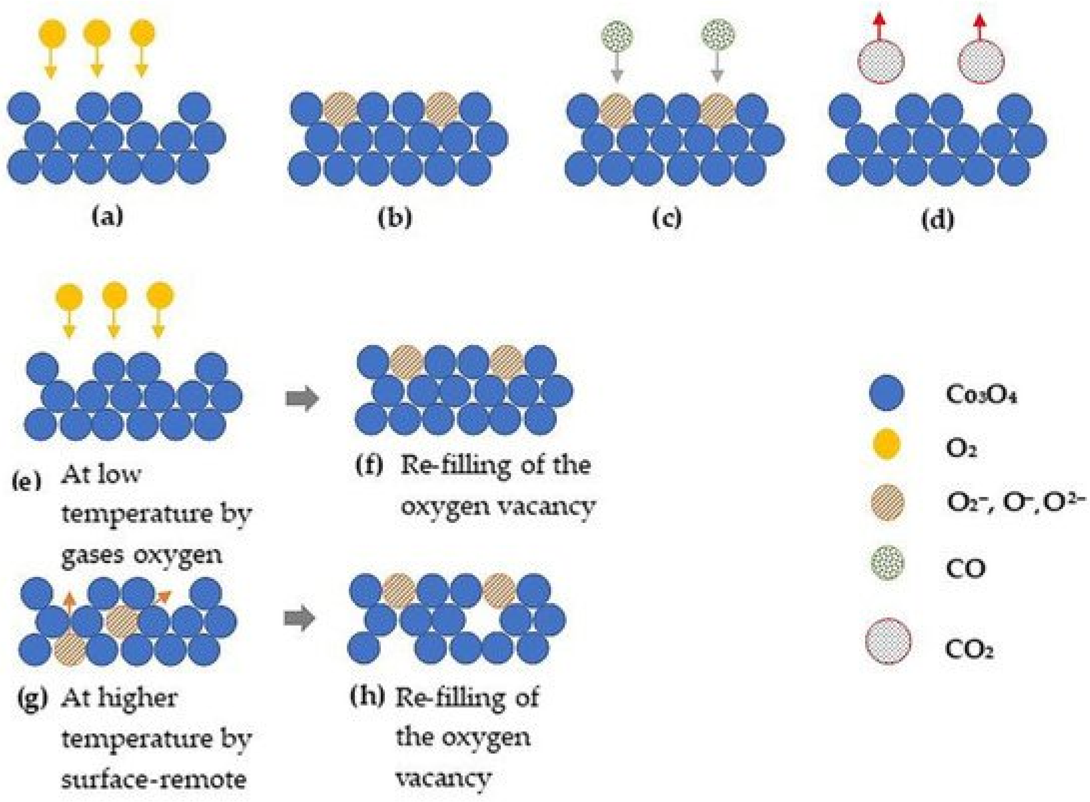

**Figure 15.** The schematics of proposed CO detection mechanism: (**a**,**b**) adsorption of $O_2$ to the $Co_3O_4$ surface; (**c**) adsorption of CO to the $Co_3O_4$ surface once it reacts with surface-near lattice oxygen; (**d**) the desorption of CO as $CO_2$; (**e**,**f**) oxygen vacancies are replenished by oxygen from the gas phase; (**g**,**h**) replenishment of oxygen vacancies by oxygen from the surface-remote lattice. Redrawn with the permission from [28].

In 2010 Patil et al. have demonstrated $Co_3O_4$ NRs sensing of CO with a response of 6.5 to 50 ppm CO at 250 °C [15]. The NRs sensors have demonstrated a higher response compared to the commercially available NP sensors due to the stronger bonding between nanoparticles in the NRs beside the higher surface-to-volume ratio. Additionally, the fabricated sensors have shown superior selectivity compared to $H_2$, LPG, $CO_2$, and ethanol.

However, CO sensing at a low working temperature (100 °C) has been reported by Dou et al. in 2014 [16]. The NFs sensors demonstrated a higher response (~13.5 ($R_g/R_a$) toward 50 ppm CO. Moreover, the detection of 5 ppm at 100 °C has been reported by the Busacca et al. on NFs $Co_3O_4$ sensors in the same year [62]. The excellent CO-sensing response of 2.4 ($R_g/R_a$) together with response time of 14 s and recovery time of 36 s of NFs was attributed to the higher effective surface area as well as the higher number of oxygen vacancies or defects on the NFs surface. Additionally, the lower crystallite size (about 15 nm) has been identified as one of the potential factors that could enhance the sensor performances. However, the sensor response was saturated at a concentration of 20 ppm at 100 °C owing to the formation of carbonates species at a low temperature that deactivates the action of $Co_3O_4$ catalysts in CO oxidation.

### 4.4. Sensing toward Toluene ($C_7H_8$) and Xylene ($C_8H_{10}$)

Toluene is another VOC widely used in paints, rubber, adhesives, and printing. Nonetheless, it is toxic, dangerous, and a neurotoxic compound that is damaging to humans even at very low concentrations (88 ppm) [27][76]. Owing to these consequences chemical/gas sensors are required to monitor toluene concentration in the afore mentioned applications.

Wang et al. have reported $Co_3O_4$ NRs-assisted gas sensors for toluene detection [27]. The grown rods-like structures were oriented from the assembly of numerous fine nanoparticles. The **Figure 16**a,b shows NRs with 40–50 nm width and cubic spinel $Co_3O_4$ phase. The sensors have shown an excellent response of 6 ($R_g/R_a$) toward 10 ppm of toluene and 35 ($R_g/R_a$) for 200 ppm at 200 °C together with response and recovery time of 90 s and 55 s respectively. Furthermore, higher sensing response has been obtained in rod-like structure, compared to nanoparticle, due to the higher amount of adsorbed oxygen molecules and the easiest diffusion of toluene through the well-aligned porous structures. This in turn improves toluene molecules absorption in the rod-like $Co_3O_4$ surface as depicted in **Figure 16**c,d. Once toluene molecules interact with the pre-adsorbed oxygen, the following reaction takes place on the surface of $Co_3O_4$:

$$C_7H_8 + 2O^- \rightarrow C_7H_6O^- + H_2O + e^- \quad (10)$$

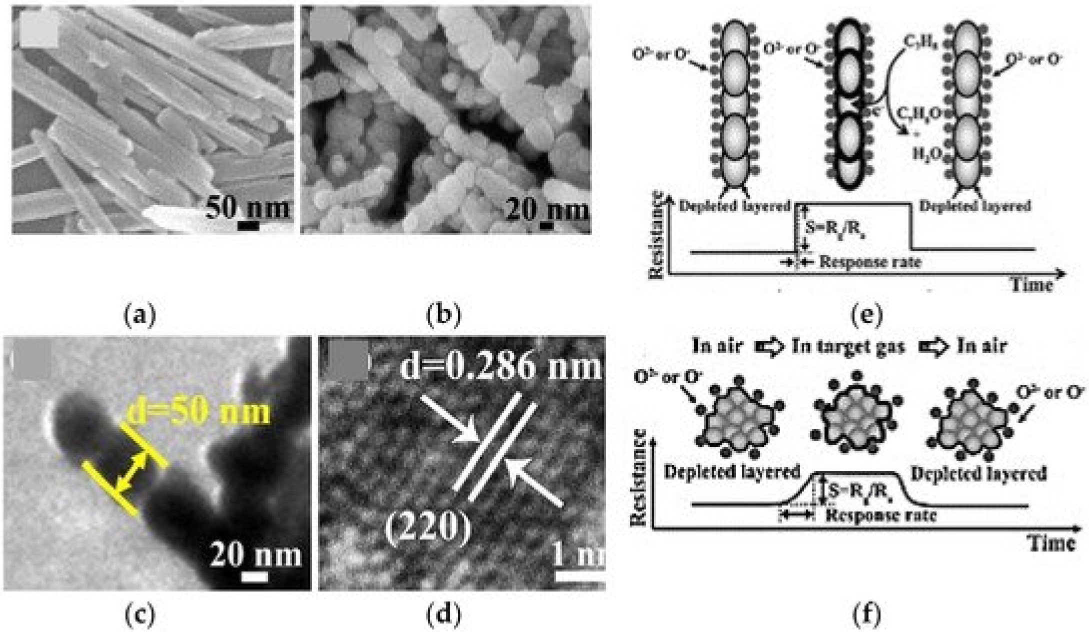

**Figure 16.** The FESEM:(**a**) as grown; (**b**) calcinated at 450 °C for 3 h; (**c**) TEM and; (**d**) HRTEM of the calcinated $Co_3O_4$ nano rods. The illustration of gas-sensing mechanism; (**e**) $Co_3O_4$ nanorods; (**f**) commercial $Co_3O_4$ powder. Reprinted with the permission from [27].

The released electron will interact with the hole in $Co_3O_4$ resulting in the decrease of the carrier concentration (hole), thus increasing the sensor resistance which can be used to study the concentration of interacting chemical compounds.

Sensing properties tunability, such as selectivity toward different gases, could be interesting when considering the production costs. The possibility to detect two gases with the same sensor exploiting different operating temperatures has been demonstrated by the Jeong et al. on Cr-incorporated $Co_3O_4$ NRs for xylene and toluene [59]. The responses to xylene of pure $Co_3O_4$ NRs and Cr-incorporated NRs were found to increase at 250 °C and the sensing properties were tuned toward the toluene as it is working at 300 °C. Additionally, the fabricated Cr incorporated sensor has shown higher selectivity of 5.61 ($S_{toluene}/S_{ethanol}$) and 6.01 ($S_{xylene}/S_{ethanol}$) in the 1.89% Cr-doped $Co_3O_4$ NRs at 275 °C for a concentration of 5 ppm. The selective sensing of toluene in Cr incorporated sensors has been attributed to the synergetic effect of abundant adsorbed oxygen on $Co_3O_4$ surface and the catalytic action of Cr for partial oxidation of methyl groups in toluene into a more reactive chemical species for xylene detection. Yet, the fastest detection of xylene was reported for $Co_3O_4$ 1D nano structures NFs by Qu et al. in [67] with a response and a recovery time of 15 s and 22 s respectively. The reported faster response and recovery times have been attributed to the fast mass transfer of xylene molecules from and to the interaction area, together with the distribution of bimodal pore sizes [67].

## 4.5. Sensing toward Ammonia ($NH_3$)

Ammonia is one of the extensively employed chemical in many fields for instance food processing, clinical diagnosis, and fertilizer production. However, direct contact or inhalation of ammonia at lower ppm levels can lead to burn of skin, eyes, lungs. Subsequently, inhalation of very high $NH_3$ concentration (10,000 ppm) for 3 h may cause death [77][78]. Hence detection of $NH_3$ is important. Beside the existing ammonia sensors that operate at high working temperature (>300 °C), an outstanding $NH_3$ sensor operating at 160 °C has been reported with the exceptional response and recovery time of 2 s and 10 s, a sensing response of 11.2 for the concentration of 100 ppm [53]. The reported sensor has been prepared with hierarchical structured $Co_3O_4$ NRs. The grown NRs were 200 nm in diameter approximately and from 1 to 2 µm in length (**Figure 17**a–c). The superior response has been ascribed to the enormous number of active sites and space in the hierarchical nanostructures for adsorption and reaction between analyte gases and adsorbed oxygen ions (**Figure 17**d) [79]. The existence of multiple HALs layers on the surface of hierarchical nano structures may be one of the reasons for this superior sensing performance toward $NH_3$. $NH_3$-sensing reaction on the $Co_3O_4$ surface can be understand as follows.

$$2NH_3 + 7O^-_{(ads)} \leftrightarrow 3H_2O + 2NO_2 + 7e^- \quad (11)$$

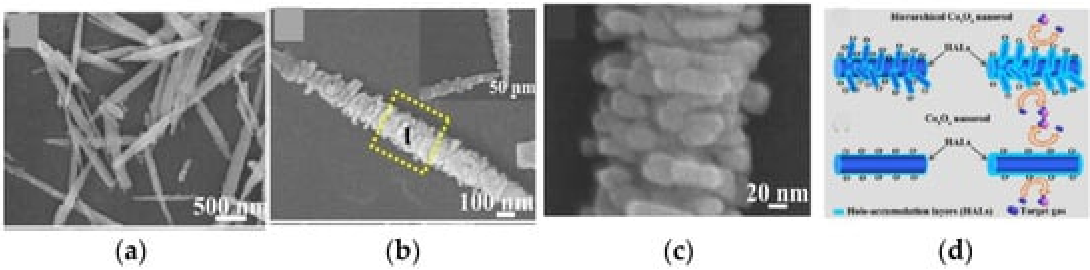

**Figure 17.** The FESEM images: (**a**–**c**) hierarchical $Co_3O_4$ nanorods; (**d**) illustration of the gas detection mechanism. Reprinted with the permission from [53].

Hence Fung et al. have demonstrated an excellent $NH_3$ sensor based on reduced graphene oxide (rGO) encapsulated $Co_3O_4$ composite nanofibers working at room temperature [71]. Fabricating a sensor that demonstrates outstanding gas detection capabilities at room temperature is among the best achievement when considering energy consumption, stability, portability, and low operation cost. There are a lot of research works focusing on low cost and stable sensors. The fabricated sensors have achieved a response of 53.6% $(R_a{-}R_g)/R_a$ together with 4 s and 5 min as response and recovery time respectively [71]. The exceptional room temperature gas-sensing performances can be ascribed to the remarkable $NH_3$ interaction with the superficial layer of rGO and the polarized C-$Co^{3+}$ covalent cores within the porous nanofibers. Furthermore, these sensors show a superior selectivity to $NH_3$ among the ethanol, methanol, formaldehyde, methylbenzene, benzene, and acetone owing to the different adsorption properties, higher polarity of $NH_3$, and the coupling effect of Co-C. The schematic illustration of the growth and gas-sensing mechanism is shown in **Figure 18**a–c.

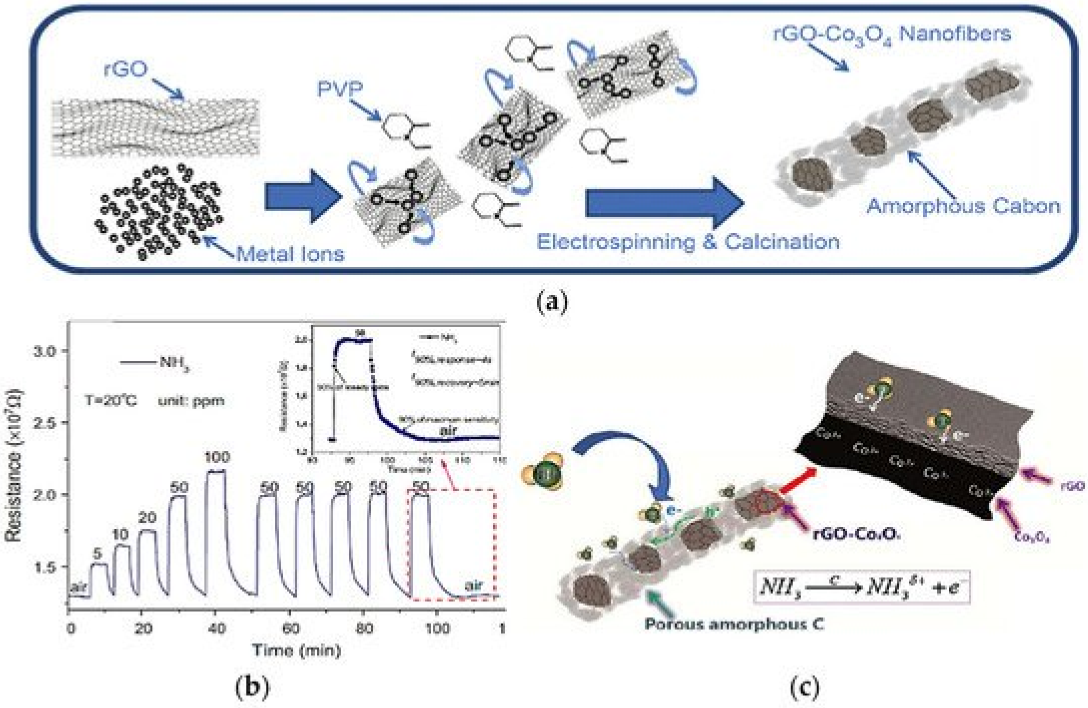

**Figure 18.** The schematic illustration of growth mechanism: (**a**) rGO-$Co_3O_4$ composite nanofibers; (**b**) dynamic response toward the $NH_3$; (**c**) schematic diagram of the sensing mechanism of the rGO–$Co_3O_4$ composite nanofibers toward ammonia at room temperature. Reprinted with the permission from [71].

## 4.6. Detection toward Hydrogen Sulfide ($H_2S$)

$H_2S$ is a colorless, irritating, and highly toxic gas. It may lead to strong effects in both visual and respiratory systems at concentrations close to 50 ppm. Furthermore, even a rapid exposure above 100 ppm may induce coma and even death due to respiratory paralysis [80][81]. Thereby, a reliable sensor for $H_2S$ detection is necessary to monitor its presence.

Fabrication of $Co_3O_4$ mesoporous nanochains sensor for $H_2S$ detection has been demonstrated in 2018 by Quang et al. [82]. The nanochains were obtained by calcinating the hydrothermal grown nanowires at 600 °C for 5 h (**Figure 19**a–c). The meso-porosity in the nanochains were ascribed to the elimination of adsorbed water molecules (justified by the total weight loss of 30.5% calcinated/as grown nanochains). The weight change was noticed in 30–200 °C and 200–400 °C temperature range in TG-DTA, corresponding to the removal of absorbed water and oxidation of $Co(CO_3)_{0.5}(OH).11H_2O$ into $Co_3O_4$. These nanochains have shown superior selectivity toward $H_2S$ among other tested gases ($NH_3$, $H_2$, and CO). Moreover, the response stability was measured over a period of five months and response and recovery time were 46 s and 24 s. Additionally, the principal mechanisms of $H_2S$ detection would be interesting to mention [Equation (11)] to conclude the discussion on $H_2S$ detection [64][72].

$$2H_2S + 3O_2^{-} \rightarrow 2H_2O + 2SO_2 + 3e^{-} \quad (12)$$

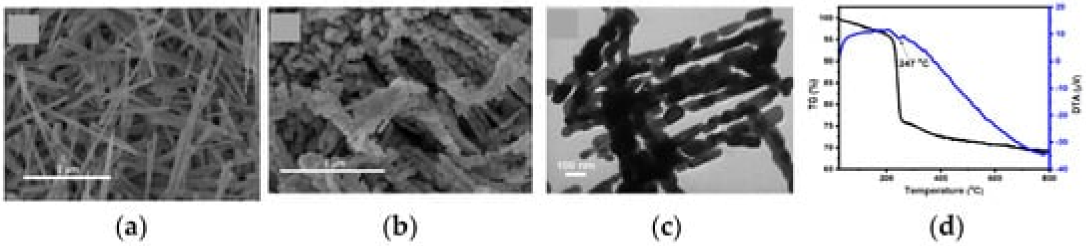

**Figure 19.** Morphological features of the mesoporous $Co_3O_4$ nanochains: (**a**) SEM; (**b**) TEM; (**c**) HRTEM images; (**d**) TG and DTA plots of cobalt carbonate hydroxide nanowire. Reprinted with the permission from [82].

## 4.7. Sensing toward Diethyl Ether ($C_4H_{10}O$, DEE)

Diethyl ether is a VOC with a pungent smell. It is extensively used as an organic solvent in diesel engine, laboratory, industry, and medicine owing to its low viscosity, and high chemical stability. However, its high volatility and low flash point induce dizziness, headaches, proteinuria, and even death in humans [30]. Recently, Jiang et al. have demonstrated the potentialities of $Co_3O_4$ NRs sensors for DEE detection [30]. They have reported a complete decomposition of $CoCO_3$ precursor at 355–600 °C in addition to the water and hydroxyl compound elimination reported by Quang et al. [82]. The prepared sensing devices have demonstrated a response of 110.34 to 100 ppm DEE at 160 °C. This excellent response was attributed to the high effective surface area and mesoporous structure resulting from the complete $CoCO_3$ decomposition. Furthermore, the mesoporous structure may facilitate both DEE molecules diffusion and adsorption on the $Co_3O_4$ surface. This in turn enhances the sensor response. A possible REDOX mechanism on the MOX surface is described in Equations (13) and (14).

$$C_2H_5OC_2H_{5(gas)} + 12O^{-} \rightarrow 4CO_2 + 5H_2O + 12e^{-} \quad (13)$$

$$e^{-} + h^{+} \rightarrow \text{Null} \quad (14)$$

The sensors have shown an interesting selectivity toward DEE compared to acetone, isopropanol, ethanol, acetonitrile, cyclohexane, chloroform, and ammonia at the same concentration.

## 4.8. Sensing toward Formaldehyde (HCHO)

Formaldehyde (aldehyde) is a carbonyl species, a colorless gas, and soluble in organic solvents. It is carcinogenic for humans [83] and one of the main reasons for “sick building syndrome” (SBS) and “new car smell.” It causes symptoms such as headache, dizziness, fatigue, and irritation of the general sensory systems and central nervous system damage. World Health Organization (WHO) has limited the exposure beyond 0.08 ppm toward HCHO even for a short-term period (30 min) to avoid sensory irritation [84]. Therefore, HCHO concentration monitoring is highly demanded in all environments.

$Co_3O_4$ hollow NTs (**Figure 20**a–d), grown from solution phase, were tested for HCHO sensing at 140–220 °C in 2014 by Wang et al. [85]. A response of ($R_g/R_a$) 6.3 at 180 °C, together with response and recovery time of 3 s and 1 s respectively, was reported for 50 ppm. The excellent sensing performances were attributed to the distinctive hollow structure and the rough surfaces of $Co_3O_4$ NTs. Meanwhile, Bai and coworkers have demonstrated excellent sensing performance toward HCHO in Au@$Co_3O_4$ composite nanowires comparted to pristine $Co_3O_4$ NWs [86]. In this study the compact NWs were synthesized via a facile hydrothermal method from the precursor $Co(CO_3)_{0.5}(OH)\cdot 0.11H_2O$ followed by annealing treatment. The nano structured annealed at 400 °C have demonstrated the highest response toward 20 ppm HCHO with a response of 17.25 ($R_g/R_a$) at an operating temperature of 90 °C. The excellent sensing features have been achieved due to the electron transfer between Ag nanoparticles in the composite and $Co_3O_4$ as well as the catalytic property of the Ag nanoparticles which accelerate the adsorption and dissociation of gas molecules to enhance the gas-sensing performance. HCHO-sensing mechanism can be described as follows [86][87].

$$HCHO_{(g)} \rightarrow HCHO_{(ads)} \quad (15)$$

$$HCHO_{(ads)} + 2O_2^{-} \rightarrow CO_2 + H_2O + 2e^{-} \quad (16)$$

$$HCHO_{(ads)} + 2O^{2-} \rightarrow CO_2 + H_2O + 4e^{-} \quad (17)$$

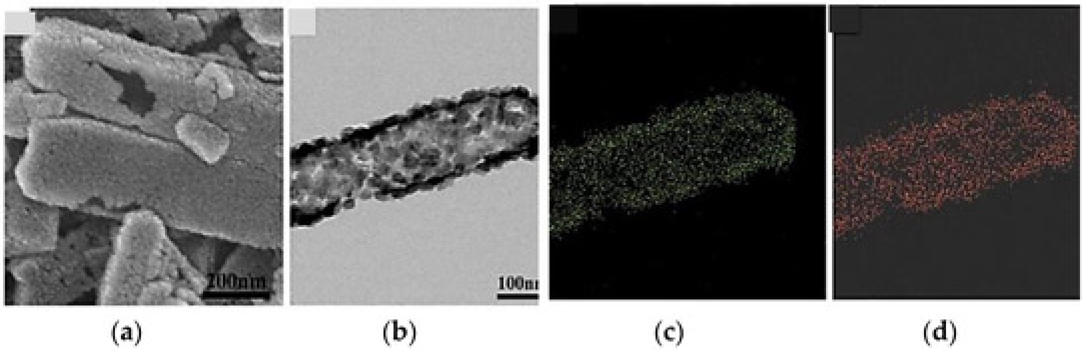

**Figure 20.** $Co_3O_4$ hollow nanotubes: (**a**) The FESEM image; (**b**) the TEM image; (**c**,**d**) elemental mapping images of Co and O, of $Co_3O_4$ hollow nanotubes. Reprinted with the permission from [85].

## 4.9. Sensing toward Dimethyl Methylphosphonate ($C_3H_9O_3P$, DMMP)

Dimethyl methylphosphonate (DMMP) is a nontoxic and organophosphorus compound which is commonly considered as a simulant for sarin. Sarin is known as a G-type nerve agent that is dangerous even a few ppm [88]. Therefore, there is an increasing demand for a reliable sarin sensor but, due to security reasons, the lab tests are normally made with DMMP. One among the different strategies, proposed to achieve its low operating temperature sensing, is the use of organic functionalized composite metal oxide nanomaterials. Furthermore, MOX surface photoactivation during the chemical interaction has been widely investigated to decrease the sensor energy consumption. In 2020 Alali et al. have proposed hexafluoroisopropanol (HFIP) functionalized $Co_3O_4$/CuO composite nanotubes as a hybrid-sensing material for DMMP detection [89]. These hybrid HFIP-$Co_3O_4$/CuO NTs have shown an excellent response (Rg/Ra) of 8.8 to 0.5 ppm of DMMP at 90 °C together with rapid response and recovery time under light irradiation (7.3 s and 5.2 s, respectively). These excellent gas-sensing performances were ascribed to both H-bonding between DMMP and HFIP groups and photo-activation (**Figure 21**a). The fast response and recovery may be justified by the hollow morphology, while the lower operating temperature by the p-p heterojunction formation which may lower the potential energy barrier. Moreover, this hybrid sensor has shown superior repeatability and stability even at 80% RH (**Figure 21**b,c). DMMP-sensing mechanism is shown in **Figure 22**a,b.

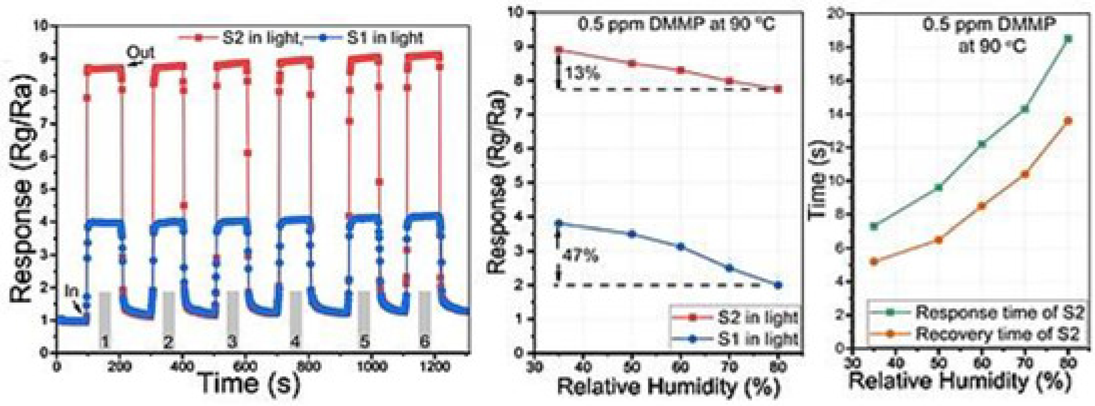

(a) (b) (c)

**Figure 21.** Dynamic response: (**a**) $Co_3O_4$/CuO NTs (S1) and hybrid HFIP-$Co_3O_4$/CuO NTs (S2) sensors toward 0.5 ppm DMMP; (**b**) responses of the S1 and S2 along with the relative humidity (RH %); (**c**) response and recovery times of S2 sensors. Reprinted with the permission from [89].

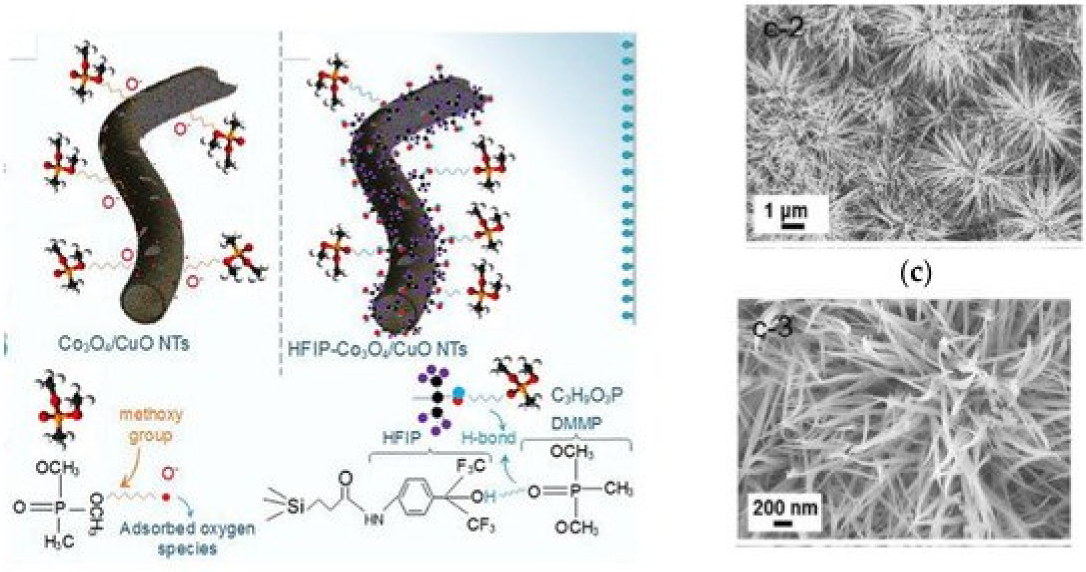

(c)

(a) (b) (d)

**Figure 22.** The schematic of DMMP-sensing mechanism: (**a**) $Co_3O_4$/CuO NTs; (**b**) hybrid HFIP-$Co_3O_4$/CuO NTs. Re-printed with the permission from [89]; (**c**,**d**) SEM micrograms of the reported NWs array. Reprinted with the permission from [22].

## 4.10. Sensing toward Triethylamine ($C_6H_{15}N$, TEA)

Triethylamine is a VOCs used as a catalytic solvent, corrosion inhibitor, hardening agent for polymers, and in many chemical syntheses processes [90]. TEA causes skin and eye burns, headaches, and particularly respiratory awkwardness because of its robust pungency, which can cause pulmonary edema and even death [90]. It is very flammable hence blending of high concentration of TEA in air can potentially end up with intensive explosions. Thereby it is important to monitor TEA in all environments.

The only study on TEA detection using $Co_3O_4$ 1D-based sensors is reported by Xu et al. [22]. In the reported study a possible alternation in density, length, and shape of $Co_3O_4$ NWs arrays has been found depending on the $NH_4F$ concentration of the chemical solution of hydrothermal process (**Figure 22**c,d). The best response toward TEA was 4 ($R_g/R_a$) at 250 °C with little interference of humidity due to its unique superficial properties and high operating temperature. Moreover, the sensor has demonstrated repeatability and stability of the sensing performances up to one month. Moreover, the sensors response ($R_g/R_a$) results toward ten gases (100 ppm) including ethanol (1.8), methanol (1.6), acetone (1.6), ethyl acetate (1.6), xylene (1.8), propanol (2.0), benzene (1.2), formaldehyde (1.6), ammonia (3.6), and butanol (2.0) have demonstrated higher selectivity to TEA. The sensing mechanism can be identified as bellow [22].

$$2N(C_2H_5)_{3(g)} + 39O^{-}_{(ads)} \rightarrow N_2 + 15H_2O + 12CO_2 + 39e^{-} \quad (18)$$

## References

1. Hulanicki, A.; Glab, S.; Ingman, F. Chemical Sensors: Definitions and Classification. Pure Appl. Chem. 1991, 63, 1247–1250.
2. Qiao, X.; Xu, Y.; Yang, K.; Ma, J.; Li, C.; Wang, H.; Jia, L. Mo Doped BiVO4 Gas Sensor with High Sensitivity and Selectivity Towards H2S. Chem. Eng. Sci. 2020, 395, 125144.
3. Choi, K.; Kim, H.; Kim, K.; Liu, D.; Cao, G.; Lee, J. C2H5OH Sensing Characteristics of Various Co3O4 Nanostructures Prepared by Solvothermal Reaction. Sens. Actuators B Chem. 2010, 146, 183–189.
4. Aqeel, T.; Galstyan, V.; Comini, E. Mesoporous Polycrystalline SnO2 Framework Synthesized by Direct Soft Templating Method for Highly Selective Detection of NO2. Nanotechnology 2019, 31, 105502.
5. Comini, E. Metal Oxide Nano-Crystals for Gas Sensing. Anal. Chim. Acta 2006, 568, 28–40.
6. Comini, E.; Yubao, L.; Brando, Y.; Sberveglieri, G. Gas Sensing Properties of MoO3 Nanorods to CO and CH3OH. Chem. Phys. Lett. 2005, 407, 368–371.

7. Wong, Y.; Ang, B.; Haseeb, A.; Baharuddin, A.; Wong, Y. Review—Conducting Polymers as Chemiresistive Gas Sensing Materials: A Review. J. Electrochem. Soc. 2019, 167, 037503.
8. Husain, A.; Ahmad, S.; Mohammad, F. Synthesis, Characterisation and Ethanol Sensing Application of Polythiophene/Graphene Nanocomposite. Mater. Chem. Phys. 2020, 239, 122324.
9. Guo, Z.; Liao, N.; Zhang, M.; Feng, A. Enhanced Gas Sensing Performance of Polyaniline Incorporated with Graphene: A First-Principles Study. Phys. Lett. A 2019, 383, 2751–2754.
10. Reddeppa, M.; Chandrakalavathi, T.; Park, B.; Murali, G.; Siranjeevi, R.; Nagaraju, G.; Su Yu, J.; Jayalakshmi, R.; Kim, S.; Kim, M. UV-Light Enhanced CO Gas Sensors Based on Ingan Nanorods Decorated With P-Phenylenediamine-Graphene Oxide Composite. Sens. Actuators B Chem. 2020, 307, 127649.
11. Harraz, F.; Faisal, M.; Jalalah, M.; Almadiy, A.; Al-Sayari, S.; Al-Assiri, M. Conducting Polythiophene/A-Fe2O3 Nanocomposite for Efficient Methanol Electrochemical Sensor. Appl. Surf. Sci. 2020, 508, 145226.
12. Choi, J.; Hwang, I.; Kim, S.; Park, J.; Park, S.; Jeong, U.; Kang, Y.; Lee, J. Design of Selective Gas Sensors Using Electrospun Pd-Doped SnO2 Hollow Nanofibers. Sens. Actuators B Chem. 2010, 150, 191–199.
13. Wang, C.; Yin, L.; Zhang, L.; Xiang, D.; Gao, R. Metal Oxide Gas Sensors: Sensitivity and Influencing Factors. Sensors 2010, 10, 2088–2106.
14. Kim, H.; Lee, J. Highly Sensitive and Selective Gas Sensors Using P-Type Oxide Semiconductors: Overview. Sens. Actuators B Chem. 2014, 192, 607–627.
15. Patil, D.; Patil, P.; Subramanian, V.; Joy, P.; Potdar, H. Highly Sensitive and Fast Responding CO Sensor Based on Co3O4 Nanorods. Talanta 2010, 81, 37–43.
16. Dou, Z.; Cao, C.; Chen, Y.; Song, W. Fabrication of Porous Co3O4 nanowires with High CO Sensing Performance at A Low Operating Temperature. Chem. Commun. 2014, 50, 14889–14891.
17. Zhang, X.; Wang, J.; Xuan, L.; Zhu, Z.; Pan, Q.; Shi, K.; Zhang, G. Novel Co3O4 Nanocrystalline Chain Material as A High Performance Gas Sensor at Room Temperature. J. Alloy. Compd. 2018, 768, 190–197.
18. Tan, J.; Dun, M.; Li, L.; Zhao, J.; Tan, W.; Lin, Z.; Huang, X. Synthesis of Hollow and Hollowed-Out Co3O4 Microspheres Assembled by Porous Ultrathin Nanosheets For Ethanol Gas Sensors: Responding and Recovering in One Second. Sens. Actuators B Chem. 2017, 249, 44–52.
19. Tan, W.; Tan, J.; Li, L.; Dun, M.; Huang, X. Nanosheets-Assembled Hollowed-Out Hierarchical Co3O4 Microrods For Fast Response/Recovery Gas Sensor. Sens. Actuators B Chem. 2017, 249, 66–75.

20. Yuan, Y.; Wang, Y.; He, X.; Chen, M.; Liu, J.; Liu, B.; Zhao, H.; Liu, S.; Yang, H. Increasing Gas Sensitivity of Co3O4 Octahedra by Tuning Co-Co3O4 (111) Surface Structure and Sensing Mechanism of 3-Coordinated Co Atom as An Active Center. J. Mater. Sci.: Mater. Electron. 2020, 31, 8852–8864.
21. Zhou, Q.; Zeng, W. Shape Control of Co3O4 Micro-Structures for High-Performance Gas Sensor. Phys. E Low Dimens. Syst. Nanostruct. 2018, 95, 121–124.
22. Xu, K.; Yu, X.; Zhao, W.; Zeng, W. Density-Dependent of Gas-Sensing Properties of Co3O4 Nanowire Arrays. Phys. E Low Dimens. Syst. Nanostruct. 2020, 118, 113956.
23. Kozlovskiy, A.; Zdorovets, M. The Study of The Structural Characteristics and Catalytic Activity of Co/CoCo2O4 Nanowires. Compos. B. Eng. 2020, 191, 107968.
24. Nguyen, H.; El-Safty, S. Meso and Macroporous Co3O4 Nanorods for Effective VOC Gas Sensors. J. Phys. Chem. C 2011, 115, 8466–8474.
25. Wen, Z.; Zhu, L.; Mei, W.; Hu, L.; Li, Y.; Sun, L.; Cai, H.; Ye, Z. Rhombus-Shaped Co3O4 Nanorod Arrays for High-Performance Gas Sensor. Sens. Actuators B Chem. 2013, 186, 172–179.
26. Wang, S.; Cao, J.; Cui, W.; Fan, L.; Li, X.; Li, D.; Zhang, T. One-Dimensional Porous Co3O4 Rectangular Rods for Enhanced Acetone Gas Sensing Properties. Sens. Actuators B Chem. 2019, 297, 126746.
27. Wang, L.; Deng, J.; Lou, Z.; Zhang, T. Nanoparticles-Assembled Co3O4 Nanorods P-Type Nanomaterials: One-Pot Synthesis and Toluene-Sensing Properties. Sens. Actuators B Chem. 2014, 201, 1–6.
28. Vetter, S.; Haffer, S.; Wagner, T.; Tiemann, M. Nanostructured Co3O4 as a CO Gas Sensor: Temperature-Dependent Behavior. Sens. Actuators B Chem. 2015, 206, 133–138.
29. Jiang, R.; Jia, L.; Guo, X.; Zhao, Z.; Du, J.; Wang, X.; Wang, P.; Xing, F. Dimethyl Sulfoxide-Assisted Hydrothermal Synthesis of Co3O4-Based Nanorods For Selective and Sensitive Diethyl Ether Sensing. Sens. Actuators B Chem. 2019, 290, 275–284.
30. Deng, S.; Liu, X.; Chen, N.; Deng, D.; Xiao, X.; Wang, Y. A Highly Sensitive VOC Gas Sensor Using P-Type Mesoporous Co3O4 Nanosheets Prepared by A Facile Chemical Coprecipitation Method. Sens. Actuators B Chem. 2016, 233, 615–623.
31. Zhang, Z.; Wen, Z.; Ye, Z.; Zhu, L. Gas Sensors Based on Ultrathin Porous Co3O4 Nanosheets to Detect Acetone at Low Temperature. RSC Adv. 2015, 5, 59976–59982.
32. Lü, Y.; Zhan, W.; He, Y.; Wang, Y.; Kong, X.; Kuang, Q.; Xie, Z.; Zheng, L. MOF-Templated Synthesis of Porous Co3O4 Concave Nanocubes with High Specific Surface Area and Their Gas Sensing Properties. ACS Appl. Mater. Interfaces 2014, 6, 4186–4195.

33. Cao, J.; Wang, S.; Zhao, X.; Xing, Y.; Li, J.; Li, D. Facile synthesis and enhanced toluene gas sensing performances of Co3O4 hollow nanosheets. Mater. Lett. 2020, 263, 127215.
34. Wen, Z.; Zhu, L.; Li, Y.; Zhang, Z.; Ye, Z. Mesoporous Co3O4 Nanoneedle Arrays for High-Performance Gas Sensor. Sens. Actuators B Chem. 2014, 203, 873–879.
35. Park, J.; Shen, X.; Wang, G. Solvothermal Synthesis and Gas-Sensing Performance of Co3O4 Hollow Nanospheres. Sens. Actuators B Chem. 2009, 136, 494–498.
36. Shen, S.; Xu, M.; Lin, D.; Pan, H. The Growth of Urchin-Like Co3O4 Directly on Sensor Substrate and Its Gas Sensing Properties. Appl. Surf. Sci. 2017, 396, 327–332.
37. Li, C.; Yin, X.; Wang, T.; Zeng, H. Morphogenesis of Highly Uniform CoCo3 Submicrometer Crystals and Their Conversion to Mesoporous for Gas-Sensing Applications. Chem. Mater. 2009, 21, 4984–4992.
38. Deng, S.; Chen, N.; Deng, D.; Li, Y.; Xing, X.; Wang, Y. Meso and Macroporous Coral-Like Co3O4 for VOCs Gas Sensor. Ceram. Int. 2015, 41, 11004–11012.
39. Lee, J. Gas Sensors Using Hierarchical and Hollow Oxide Nanostructures: Overview. Sens. Actuators B Chem. 2009, 140, 319–336.
40. Xu, J.; Zhang, Y.; Chen, Y.; Xiang, Q.; Pan, Q.; Shi, L. Uniform ZnO Nanorods Can be Used to Improve the Response of ZnO Gas Sensor. Mater. Sci. Eng. B 2008, 150, 55–60.
41. Xu, J.; Wang, D.; Qin, L.; Yu, W.; Pan, Q. SnO2 Nanorods and Hollow Spheres: Controlled Synthesis and Gas Sensing Properties. Sens. Actuators B Chem. 2009, 137, 490–495.
42. Wang, L.; Song, S.Y.; Hong, B.; Xu, J.C.; Han, Y.B.; Jin, H.X.; Jin, D.F.; Li, J.; Yang, Y.T.; Peng, X.L.; et al. Highly improved toluene gas-sensing performance of mesoporous Co3O4 nanowires and physical mechanism. Mater. Res. Bull 2021, 140, 111329.
43. Qiao, X.; Ma, C.; Chang, X.; Li, X.; Li, K.; Zhu, L.; Xia, F.; Xue, Q. 3D radial Co3O4 nanorod cluster derived from cobalt-based layered hydroxide metal salt for enhanced trace acetone detection. Sens. Actuators B Chem. 2021, 324, 128926.
44. Xu, J.; Cheng, J. The Advances of Co3O4 as Gas Sensing Materials: A Review. J. Alloy. Compd. 2016, 686, 753–768.
45. Chen, J.; Wu, X.; Selloni, A. Electronic structure and bonding properties of cobalt oxide in the spinel structure. Phys. Rev. B. 2011, 83, 245204.
46. Kaur, N.; Singh, M.; Moumen, A.; Duina, G.; Comini, E. 1D Titanium Dioxide: Achievements in Chemical Sensing. Materials 2020, 13, 2974.
47. Bagga, S.; Akhtar, J.; Mishra, S. Synthesis and Applications of ZnO Nanowire: A Review. AIP Conf. Proc. 2018, 1989, 020004.

48. Moseley, P. Progress in the Development of Semiconducting Metal Oxide Gas Sensors: A Review. Meas. Sci. Technol. 2017, 28, 082001.
49. Barsan, N.; Simion, C.; Heine, T.; Pokhrel, S.; Weimar, U. Modeling of Sensing and Transduction for P-Type Semiconducting Metal Oxide Based Gas Sensors. J. Electroceram. 2009, 25, 11–19.
50. Barsan, N.; Weimar, U. Conduction Model of Metal Oxide Gas Sensors. J. Electroceram. 2001, 7, 143–167.
51. Mijatovic, D.; Eijkel, J.; van den Berg, A. Technologies for Nanofluidic Systems: Top-Down vs. Bottom-Up—A Review. Lab Chip 2005, 5, 492.
52. Cao, J.; Wang, S.; Zhang, H.; Zhang, T. Constructing One Dimensional Co3O4 Hierarchical Nanofibers as Efficient Sensing Materials for Rapid Acetone Gas Detection. J. Alloy. Compd. 2019, 799, 513–520.
53. Deng, J.; Zhang, R.; Wang, L.; Lou, Z.; Zhang, T. Enhanced Sensing Performance of The Co3O4 Hierarchical Nanorods To NH3 Gas. Sens. Actuators B Chem. 2015, 209, 449–455.
54. George, G.; Anandhan, S. Tuning Characteristics of Co3O4 Nanofiber Mats Developed for Electrochemical Sensing of Glucose and H2O2. Thin Solid Films 2016, 610, 48–57.
55. Sun, C.; Su, X.; Xiao, F.; Niu, C.; Wang, J. Synthesis of Nearly Monodisperse Co3O4 Properties. Sens. Actuators B Chem. 2011, 157, 681–685.
56. Xu, K.; Zou, J.; Tian, S.; Yang, Y.; Zeng, F.; Yu, T.; Zhang, Y.; Jie, X.; Yuan, C. Single-Crystalline Porous Nanosheets Assembled Hierarchical Co3O4 Microspheres for Enhanced Gas-Sensing Properties to Trace Xylene. Sens. Actuators B Chem. 2017, 246, 68–77.
57. Feng, S.; Li, G. Hydrothermal and Solvothermal Syntheses. In Modern Inorganic Synthetic Chemistry, 2nd ed.; Xu, R., Xu, R., Eds.; John Fedor: Cambridge, CA, USA, 2017; pp. 73–104.
58. Wang, X.; Hu, A.; Meng, C.; Wu, C.; Yang, S.; Hong, X. Recent Advance in Co3O4 and Co3O4-Containing Electrode Materials for High-Performance Supercapacitors. Molecules 2020, 25, 269.
59. Jeong, H.; Kim, H.; Rai, P.; Yoon, J.; Lee, J. Cr-Doped Co3O4 Nanorods as Chemiresistor for Ultraselective Monitoring of Methyl Benzene. Sens. Actuators B Chem. 2014, 201, 482–489.
60. Koo, A.; Yoo, R.; Woo, S.; Lee, H.; Lee, W. Enhanced Acetone-Sensing Properties of Pt-Decorated Al-Doped Zno Nanoparticles. Sens. Actuators B Chem. 2019, 280, 109–119.
61. Bhardwaj, N.; Kundu, S. Electrospinning: A Fascinating Fiber Fabrication Technique. Biotechnol. Adv. 2010, 28, 325–347.
62. Busacca, C.; Donato, A.; Lo Faro, M.; Malara, A.; Neri, G.; Trocino, S. CO Gas Sensing Performance of Electrospun Co3O4 Nanostructures at Low Operating Temperature. Sens. Actuators B Chem. 2020, 303, 127193.

63. Yoon, J.; Kim, H.; Jeong, H.; Lee, J. Gas Sensing Characteristics of P-Type Cr2O3 and Co3O4 Nanofibers Depending on Inter-Particle Connectivity. Sens. Actuators B Chem. 2014, 202, 263–271.
64. Shankar, P.; Bosco, J.; Rayappan, B. Gas sensing mechanism of metal oxides: The role of ambient atmosphere, type of semiconductor and gases—A review. Sci. Jet 2015, 4, 126.
65. Yoon, J.; Choi, J.; Lee, J. Design of a Highly Sensitive and Selective C2H5OH Sensor Using P-Type Co3O4 Nanofibers. Sens. Actuators B Chem. 2012, 161, 570–577.
66. Choi, S.; Ryu, W.; Kim, S.; Cho, H.; Kim, I. Bi-Functional Co-Sensitization of Graphene Oxide Sheets and Ir Nanoparticles on P-Type Co3O4 Nanofibers for Selective Acetone Detection. J. Mater. Chem. B 2014, 2, 7160–7167.
67. Qu, F.; Feng, C.; Li, C.; Li, W.; Wen, S.; Ruan, S.; Zhang, H. Preparation and Xylene-Sensing Properties of Co3O4 nanofibers. Int. J. Appl. Ceram. Technol. 2013, 11, 619–625.
68. Shin, J.; Choi, S.; Youn, D.; Kim, I. Exhaled Vocs Sensing Properties of WO3 Nanofibers Functionalized by Pt and IrO2 Nanoparticles for Diagnosis of Diabetes and Halitosis. J. Electroceramics 2012, 29, 106–116.
69. Brugha, R.; Edmondson, C.; Davies, J. Outdoor Air Pollution and Cystic Fibrosis. Paediatr. Respir. Rev. 2018, 28, 80–86.
70. Mirzaei, A.; Lee, J.; Majhi, S.; Weber, M.; Bechelany, M.; Kim, H.; Kim, S. Resistive Gas Sensors Based on Metal-Oxide Nanowires. J. Appl. Phys. 2019, 126, 241102.
71. Feng, Q.; Li, X.; Wang, J.; Gaskov, A. Reduced Graphene Oxide (RGO) Encapsulated Co3O4 Composite Nanofibers for Highly Selective Ammonia Sensors. Sens. Actuators B Chem. 2016, 222, 864–870.
72. Wang, M.; Zhu, Y.; Meng, D.; Wang, K.; Wang, C. A Novel Room Temperature Ethanol Gas Sensor Based on 3D Hierarchical Flower-Like TiO2 Microstructures. Mater. Lett. 2020, 277, 128372.
73. Thungon, P.; Kakoti, A.; Ngashangva, L.; Goswami, P. Advances in Developing Rapid, Reliable and Portable Detection Systems for Alcohol. Biosens. Bioelectron. 2017, 97, 83–99.
74. Mirzaei, A.; Janghorban, K.; Hashemi, B.; Bonyani, M.; Leonardi, S.; Neri, G. Highly Stable and Selective Ethanol Sensor Based on Α-Fe2O3 Nanoparticles Prepared by Pechini Sol–Gel Method. Ceram. Int. 2016, 42, 6136–6144.
75. Deng, C.; Zhang, J.; Yu, X.; Zhang, W.; Zhang, X. Determination of acetone in human breath by gas chromatography–mass spectrometry and solid-phase microextraction with on-fiber derivatization. J. Chromatogr. B 2004, 810, 269–275.

76. Ma, H.; Xu, Y.; Rong, Z.; Cheng, X.; Gao, S.; Zhang, X.; Zhao, H.; Huo, L. Highly Toluene Sensing Performance Based on Monodispersed Cr2O3 Porous Microspheres. Sens. Actuators B Chem. 2012, 174, 325–331.

77. Kwak, D.; Lei, Y.; Maric, R. Ammonia gas sensors: A comprehensive review. Talanta 2019, 204, 713–730.

78. National Research Council. Acute Exposure Guideline Levels for Selected Airborne Chemicals; National Academies Press: Washington, DC, USA, 2008; Volume 6.

79. Balamurugan, C.; Lee, D. A Selective NH3 Gas Sensor Based on Mesoporous P-Type NiV2O6 Semiconducting Nanorods Synthesized Using Solution Method. Sens. Actuators B Chem. 2014, 192, 414–422.

80. Sun, M.; Yu, H.; Dong, X.; Xia, L.; Yang, Y. Sedum Lineare Flower-Like Ordered Mesoporous In2O3/Zno Gas Sensing Materials with high Sensitive Response to H2S at Room Temperature Prepared by Self-Assembled of 2D Nanosheets. J. Alloy. Compd. 2020, 844, 156170.

81. Zhong, K.; Chen, L.; Yan, X.; Tang, Y.; Hou, S.; Li, X.; Tang, L. Dual-Functional Multi-Application Probe: Rapid Detection of H2S And Colorimetric Recognition of HSO3—In Food and Cell. Dyes Pigments 2020, 182, 108656.

82. Quang, P.; Cuong, N.; Hoa, T.; Long, H.; Hung, C.; Le, D.; Hieu, N. Simple Post-Synthesis of Mesoporous P-Type Co3O4 Nanochains for Enhanced H2S Gas Sensing Performance. Sens. Actuators B Chem. 2018, 270, 158–166.

83. Song, M.; Choi, J.; Jeong, H.; Song, K.; Jeon, S.; Cha, J.; Baeck, S.; Shim, S.; Qian, Y. A Comprehensive Study of Various Amine-Functionalized Graphene Oxides for Room Temperature Formaldehyde Gas Detection: Experimental and Theoretical Approaches. Appl. Surf. Sci. 2020, 529, 147189.

84. Zhu, L.; Wang, J.; Liu, J.; Nasir, M.; Zhu, J.; Li, S.; Liang, J.; Yan, W. Smart Formaldehyde Detection Enabled by Metal Organic Framework-Derived Doped Electrospun Hollow Nanofibers. Sens. Actuators B Chem. 2021, 326, 128819.

85. Wang, S.; Xiao, C.; Wang, P.; Li, Z.; Xiao, B.; Zhao, R.; Yang, T.; Zhang, M. Co3O4 Hollow Nanotubes: Facile Synthesis and Gas Sensing Properties. Mater. Lett. 2014, 137, 289–292.

86. Bai, S.; Liu, H.; Sun, J.; Tian, Y.; Luo, R.; Li, D.; Chen, A. Mechanism of enhancing the formaldehyde sensing properties of Co3O4via Ag modification. RSC Adv. 2015, 5, 48619–48625.

87. Hurtado, I.D.; Chávarri, J.G.; Morandi, S.; Samà, J.; Rodríguez, A.R.; Castaño, E.; Mandayo, G.G. Formaldehyde sensing mechanism of SnO2 nanowires grown on-chip by sputtering techniques. RSC Adv. 2016, 6, 18558–18566.

88. Yang, X.; Yu, Q.; Zhang, S.; Sun, P.; Lu, H.; Yan, X.; Liu, F.; Zhou, X.; Liang, X.; Gao, Y.; et al. Highly sensitive and selective triethylamine gas sensor based on porous SnO2/Zn2SnO4 composites. Sens. Actuators B Chem. 2018, 266, 213–220.
89. Alali, K.; Liu, J.; Moharram, D.; Liu, Q.; Yu, J.; Chen, R.; Li, R.; Wang, J. Fabrication of Electrospun Co3O4/CuO P-P Heterojunctions Nanotubes Functionalized with HFIP for Detecting Chemical Nerve Agent Under Visible Light Irradiation. Sens. Actuators B Chem. 2020, 314, 128076.
90. Gui, Y.; Tian, K.; Liu, J.; Yang, L.; Zhang, H.; Wang, Y. Superior Triethylamine Detection at Room Temperature By {-112} Faceted WO3 Gas Sensor. J. Hazard. Mater. 2019, 380, 120876.

Retrieved from https://encyclopedia.pub/entry/history/show/30206